

SP-MoMamba: Superpixel-driven Mixture of State Space Experts for Efficient Image Super-Resolution

Wenbin Zou*, Yawen Cui, Yi Wang*, *Member, IEEE*, Lap-Pui Chau, *Fellow, IEEE*, Liang Chen, Jinshan Pan, *Senior Member, IEEE*, Huiping Zhuang*,[†], *Member, IEEE*, Guanbin Li, *Member, IEEE*

Abstract—State space models (SSMs) have emerged as a powerful paradigm for efficient single-image super-resolution (SR) due to their linear complexity and long-range modeling capabilities. However, existing Mamba-based methods typically rely on data-agnostic rigid scanning, which reshapes 2D images into 1D sequences over a fixed grid, inevitably disrupting spatial-semantic topology and introducing artifacts. Inspired by the Gestalt perceptual grouping theory, we propose SP-MoMamba, a superpixel-driven mixture of state space experts designed for content-aware SR. Our core idea is to transform the traditional rigid scanning into a semantic-level interaction by treating superpixels as fundamental units. Specifically, we introduce the Superpixel-driven State Space Model (SP-SSM), which compresses semantically homogeneous regions into high-order tokens to preserve global topological consistency. To address the conflict between fixed scanning scales and diverse semantic granularities, we develop the Multi-Scale Superpixel Mixture of State Space Experts (MSS-MoE). This module utilizes a dynamic routing mechanism to adaptively assign scale-specific experts, effectively capturing multi-scale textures while reducing computational redundancy. Furthermore, to prevent the loss of high-frequency details during global abstraction, we introduce a Local Spatial Modulation Expert (LSME) to complement the global modeling, ensuring a precise reconstruction of sharp edges and fine structures. Extensive experiments on standard benchmarks demonstrate that SP-MoMamba achieves superior reconstruction fidelity and a more favorable efficiency-performance trade-off compared to state-of-the-art efficient SR methods.

[†] *Corresponding Author: Huiping Zhuang*

* Joint Supervision. Wenbin Zou is with the Shien-Ming Wu School of Intelligent Engineering, South China University of Technology, Guangzhou, China, and jointly with the Department of Electrical and Electronic Engineering, The Hong Kong Polytechnic University, Hong Kong SAR, under the joint Ph.D. program supervised by Prof. Huiping Zhuang and Prof. Yi Wang. (e-mail: alex14.zou@connect.polyu.hk)

Yawen Cui, Yi Wang, and Lap-pui Chau are with the Department of Electrical and Electronic Engineering, The Hong Kong Polytechnic University, Hong Kong. (e-mail: yawencui@polyu.edu.hk, yi-eie.wang@polyu.edu.hk, lap-pui.chau@polyu.edu.hk)

Liang Chen is with the College of Photonic and Electronic Engineering, Fujian Normal University, Fuzhou, China. (e-mail: cl_0827@126.com)

Jinshan Pan is with the School of Computer Science and Engineering, Nanjing University of Science and Technology, Nanjing, China. (e-mail: jsfan@njst.edu.cn)

Huiping Zhuang is with the Shien-Ming Wu School of Intelligent Engineering, South China University of Technology, Guangzhou, China. (e-mail: hpzhuang@scut.edu.cn)

Guanbin Li is with the School of Computer Science and Engineering, Sun Yat-sen University, Guangzhou, China. (e-mail: liguanbin@mail.sysu.edu.cn)

This research was supported by the National Natural Science Foundation of China (62306117), the Guangdong Basic and Applied Basic Research Foundation (2026A1515011478), and GJYC program of Guangzhou (2024D03J0005). The research work described in this paper was conducted in the JC STEM Lab of Machine Learning and Computer Vision funded by The Hong Kong Jockey Club Charities Trust. This research received partially support from the Global STEM Professorship Scheme from the Hong Kong Special Administrative Region.

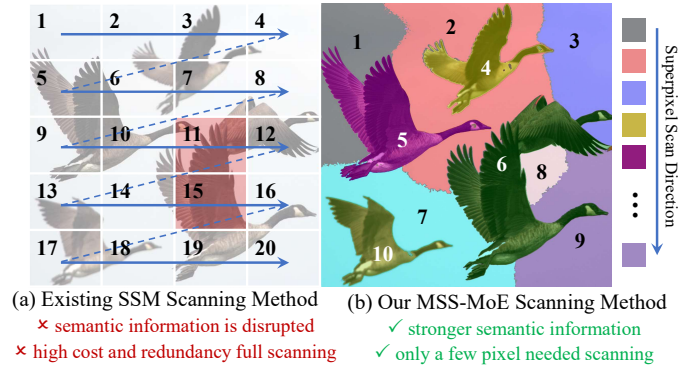


Fig. 1: (a) The existing method [11] suffers from the adverse effects of the scanning method of Mamba (the multi-directional scans are not shown for presentation clarity). (b) The proposed SP-SSM scanning method use superpixel clustering to shorten sequences for efficient global interaction in SSM, and utilizes soft mapping to accurately restore 2D spatial topology.

Index Terms—Efficient Image Super-resolution, State Space Model, Mixture-of-expert.

I. INTRODUCTION

SINGLE image super-resolution (SR) is a fundamental technique in image processing, designed to reconstruct high-resolution (HR) images from low-resolution (LR) counterparts, thereby enhancing image detail and visual quality. This technology is widely applied across diverse fields, including medical imaging, surveillance systems, and satellite imagery. Numerous studies have leveraged convolutional neural networks (CNNs) [1]–[3] and Transformers [4]–[6] to learn this inherently ill-posed mapping relationship. However, the majority of SR methods [2], [3] rely on deep and complex architectures to achieve superior performance. These approaches often entail high computational complexity, rendering real-time processing impractical on resource-constrained devices, which limits their deployment and widespread adoption in real-world scenarios. Although researchers have attempted to reduce computational complexity through techniques such as neural architecture search [7], recursive networks [8], and model distillation [9], [10], these efforts have not yet fully resolved the efficiency bottleneck.

Recently, State Space Models (SSMs), exemplified by Mamba [12], have opened new avenues for efficient SR. Mamba offers linear computational complexity and excels

at modeling long sequences, initially demonstrating its value in high-level vision tasks such as image classification [13], [14] and object detection [15], [16]. Building on this success, researchers have adapted Mamba for low-level vision tasks, including image denoising [11], image SR [17], and low-light image enhancement [18], [19]. For instance, MambaIR [11], based on a visual SSM framework, achieves reconstruction quality comparable to Transformer-based methods while maintaining lower computational costs. These developments demonstrate that Mamba effectively balances performance and efficiency in efficient SR; however, further optimizations are required to tailor the architecture to specific use cases and achieve an optimal trade-off between performance and efficiency.

Existing Mamba-based SR methods suffer from three key limitations, namely topology-disruptive scanning, fixed-scale semantic modeling, and insufficient preservation of high-frequency details. First, **the conventional scanning process suffers from inherent inefficiency and the destruction of spatial semantic topology.** Specifically, existing approaches typically employ two-dimensional selective scanning to process images, such as multi-directional [11] or cross-scanning [19]. These methods are essentially data-agnostic rigid scanning operations. As illustrated in Fig. 1(a), they forcibly flatten images into one-dimensional sequences over a fixed 2D grid. These operations not only introduces substantial computational redundancy but also severely dissociates pixels that are spatially adjacent and semantically similar, thereby disregarding the intrinsic semantic boundaries and manifold structures of natural images. Second, **a conflict exists between the single scanning scale and the diverse semantic granularities.** Natural images possess highly complex multi-scale characteristics, ranging from large-scale regions like the sky to intricate grid textures. Most existing SSMs [17], [20], [21] utilize fixed-scale receptive fields for sequential scanning, which prevents the adaptive adjustment of modeling granularity according to the semantic complexity of local content. Consequently, these models are prone to semantic confusion when processing regions with repetitive textures. Finally, **global feature computation tends to weaken local high-frequency details.** Although SSMs excel at capturing global long-range dependencies, the local high-frequency spatial details that determine image sharpness, such as edges and abrupt transitions, are often smoothed or neglected during the extreme compression inherent in long-sequence mapping.

To address the aforementioned challenges, we inspired from the perceptual grouping theory in Gestalt psychology [22], which describes the innate tendency of the human visual system to automatically aggregate discrete pixels into coherent wholes based on similarity and proximity. We propose SP-MoMamba, a superpixel-driven mixture of state space experts model tailored for efficient SR. The core idea is to transform the data-agnostic rigid scanning in SSMs into content-aware semantic-level scanning by performing semantic dimensionality reduction on the visual manifold. Specifically, SP-MoMamba consists of stacked Layers of Experts (LoE), where each LoE decouples and modulates features at both macro and micro levels. First, to avoid the destruction of

spatial continuity in existing rigid scanning, we introduce the **Superpixel-driven State Space Model (SP-SSM)**. By simulating the perceptual grouping process, this module treats clusters of pixels that are semantically homogeneous and spatially adjacent (i.e., superpixels) as an information bottleneck, dynamically compressing them into individual semantic tokens, as illustrated in Fig. 1(b). This design fundamentally adheres to the Gestalt principle of continuity, preventing the fragmentation of semantic connections during serialization and filtering redundant information, thereby enabling the SSM to focus precisely on global core semantic interactions. Second, to handle multi-scale semantic features, we design the **Multi-scale Superpixel Mixture of State Space Experts (MSS-MoE)** module. This module incorporates a dynamic routing mechanism that reflects the hierarchy of perceptual grouping, adaptively assigning scale-specific experts according to the semantic granularity of the input features. This demand-driven computing paradigm enables the model to accurately match textural features across various scales, effectively avoiding semantic confusion. Third, following the Gestalt principle that the whole is not equal to the sum of its parts, we further introduce the **Local Spatial Modulation Expert (LSME)** alongside the Superpixel Global Modulating Expert (SGME) for building long-range consistency. While SGME constructs long-range coherence, LSME focuses on capturing local topological features and high-frequency details often neglected by global abstract modeling. This decoupling mechanism facilitates both accurate global structural understanding and precise local detail reconstruction. Our contributions are summarized as follows:

- To the best of our knowledge, SP-MoMamba is among the first attempts to introduce superpixel-driven semantic grouping into state-space modeling for low-level vision. We innovatively propose the Superpixel-driven State Space Model (SP-SSM), which compresses dense pixel-level signals into higher-order semantic tokens. This paradigm substantially alleviates the spatial semantic fragmentation bottleneck caused by rigid exhaustive scanning in existing Mamba-based methods, achieving genuine content-aware processing with global topology preservation.
- To handle the scale-varying features present in natural images, we design the Multi-Scale Superpixel State Space Mixture-of-Experts module (MSS-MoE) with dynamic routing. This mechanism simulates multi-level perceptual grouping and adaptively assigns the most suitable scale experts according to the semantic complexity of local regions, avoiding semantic confusion across multi-scale features while balancing computational efficiency and multi-level semantic fidelity.
- Extensive quantitative and qualitative experiments demonstrate that SP-MoMamba substantially outperforms existing efficient SR methods in reconstruction fidelity while achieving a superior balance in inference efficiency and parameter count.

II. RELATED WORKS

A. Deep Networks for Image Super-resolution

Following the introduction of SRCNN [1], which pioneered the application of convolutional neural networks to the field of image SR and achieved remarkable success, a growing number of researchers [2], [3], [23], [24] have explored the integration of advanced deep learning architectures into this domain. For example, VDSR [25] and EDSR [2] employed residual learning to deepen network architectures, significantly enhancing the quality of image restoration. Subsequently, leveraging the exceptional performance of Transformers in high-level tasks, SwinIR [4] incorporated the local window self-attention and shift mechanisms of the Swin Transformer [26] into image restoration, further improving the quality of reconstructed images. Inspired by the success of SwinIR, researchers have focused on designing sophisticated self-attention mechanisms, such as ART [27], OminiSR [28], and GRL [5], to capture global information more effectively. Although these methods achieve impressive metric scores, they often demand substantial computational resources and a large number of parameters, posing challenges to their practical deployment on resource-constrained edge devices.

B. Efficient Super-resolution Methods

In the pursuit of more efficient models, researchers have introduced lightweight architectures [10], [29], [30] and efficient Transformers [31]–[33]. For instance, CARN [29] proposes a cascading mechanism that integrates local and global features to enhance network efficiency. IMDN [10] employs a feature distillation approach to split and aggregate features, further reducing both parameter count and computational load. SAFMN [30] improves network efficiency by constructing a feature pyramid based on channel utilization. Meanwhile, to mitigate the high complexity introduced by Transformer architectures, ELAN [31] and ESRT [32] reduce feature dimensionality through segmentation or scaling, thereby improving computational efficiency. And SCET [33] further minimizes computational costs by designing a pixel attention mechanism and an efficient Transformer module. More recently, SPIN [34] leverages superpixel attention to decrease the computational burden of Transformers while employing cross-attention to simultaneously capture local and global information. Although these methods are lightweight and efficient, there remains room for improvement in balancing the trade-off between efficiency and performance.

C. Mamba for Image Restoration

State Space Models (SSMs) have garnered significant attention from researchers due to their capability for long-range modeling and linear computational complexity. Recently, Mamba [12], a selective SSM, has been successfully adapted to the vision domain in architectures such as VMamba [13] and VIM [14]. Subsequently, its application has been further explored in low-level vision tasks, yielding a variety of methods [18], [19] with promising results. For instance, MambaIR [11] leverages the VMamba architecture to capture

spatially localized information while employing channel attention to enhance inter-channel interactions, thereby demonstrating superior performance across diverse restoration tasks. Although these methods have outperformed Transformer-based approaches, they rely on multi-directional scanning strategies to process all pixels and model corresponding spatial relationships. This reliance not only disrupts the semantic coherence of the image but also significantly increases computational overhead.

Consequently, optimizing scanning mechanisms to preserve two-dimensional spatial structures has emerged as a pivotal research focus. MambaIRv2 [20] introduces Attention-guided State-space Equations (ASE) and a Semantic-Guided Neighborhood (SGN) mechanism, endowing Mamba with non-causal modeling capabilities similar to Vision Transformers (ViTs) to mitigate long-range decay relative to scanning order. Furthermore, EVSSM [21] utilizes geometric transformations to enhance the scanning process, improving non-local information acquisition without additional computational overhead, while C2SSM [35] proposes a clustering-centroid scanning paradigm to compress millions of pixels into sparse semantic centroids for high-definition image processing. Although these methods refine efficiency or causality, they remain constrained by rigid pixel-wise traversal or the coarse weight diffusion of abstract centroids, failing to precisely align with the intrinsic topological boundaries of the image. In contrast, inspired by the Gestalt theory of perceptual grouping, our proposed SP-MoMamba introduces a Superpixel-driven State Space Model (SP-SSM). By restructuring semantically homogeneous and physically adjacent regions into high-order semantic tokens, SP-MoMamba facilitates a paradigm shift from data-agnostic rigid scanning to content-aware scanning, thereby maximizing the preservation of semantic topological integrity. Moreover, unlike the fixed granularity in C2SSM, our Multi-Scale Superpixel Mixture of State Space Experts (MSS-MoE) adaptively adjusts scanning scales via a dynamic routing mechanism, complemented by a Local Spatial Modulation Expert (LSME) to accurately compensate for high-frequency details. This method enables SP-MoMamba to achieve state-of-the-art (SOTA) reconstruction accuracy on complex datasets like Urban100 while maintaining extreme inference efficiency.

D. Mixture of Experts (MoE)

The Mixture of Experts (MoE) paradigm has gained widespread adoption in large-scale language models due to its efficiency and scalability. Consequently, MoE has been extended to advanced vision tasks, including image classification [36] and object detection [37], as well as low-level vision tasks [38]–[40]. For instance, studies [38] and [41] extract latent degradation features to construct MoE-based adaptive networks, effectively addressing diverse degradation patterns in blind SR. SeemoRe [39] employs rank-modulated experts to prioritize features with the highest information content, followed by spatial modulation experts to achieve precise spatial enhancement. Similarly, Swin2-MoSE [40] enhances Swin2SR [42] by incorporating an MoE framework, yielding improved visual outcomes. While these methods leverage the

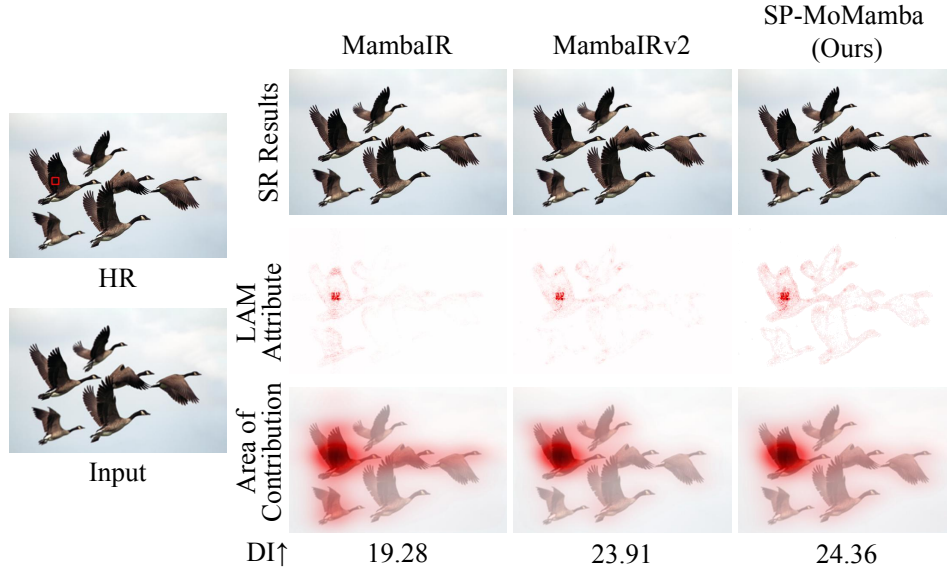


Fig. 2: Analysis semantic preservation capability of different methods. The larger the Diffusion Index (DI), the more semantically similar pixels are involved in restoring the corresponding region.

flexibility and efficiency of MoE to achieve commendable performance, there remains potential for further improvement in the quality of SR reconstruction.

III. MOTIVATION

A. State Space Models

State Space Models (SSMs) [12] are mathematical models used in control theory and signal processing to describe dynamic systems. The following equations define standard SSMs:

$$h'(t) = \mathbf{A}h(t) + \mathbf{B}x(t) \quad (1)$$

$$y(t) = \mathbf{C}h(t) + \mathbf{D}x(t) \quad (2)$$

where \mathbf{A} , \mathbf{B} , \mathbf{C} , and \mathbf{D} represent the system parameters. The terms $x(t)$, $h(t)$, and $y(t)$ denote the input, hidden state, and output, respectively. In the context of deep learning, existing SSM-based methods, such as Mamba, employ a zero-order hold (ZOH) to discretize continuous state space equations. This discretization enables the efficient processing of long sequence data and is applicable to various sequence modeling tasks. The discrete representation is governed by the following equations:

$$h_t = \bar{\mathbf{A}}h_{t-1} + \bar{\mathbf{B}}x_t \quad (3)$$

$$y_t = \mathbf{C}h_t + \mathbf{D}x_t \quad (4)$$

$$\bar{\mathbf{A}} = \exp(\Delta\mathbf{A}) \quad (5)$$

$$\bar{\mathbf{B}} = (\Delta\mathbf{A})^{-1}(\exp(\Delta\mathbf{A}) - \mathbf{I})(\Delta\mathbf{B}) \quad (6)$$

where $\bar{\mathbf{A}}$ and $\bar{\mathbf{B}}$ are the discrete counterparts of \mathbf{A} and \mathbf{B} . The symbol Δ denotes the discretization timescale parameter, which is utilized to transform the continuous parameters \mathbf{A} and \mathbf{B} into their discrete forms $\bar{\mathbf{A}}$ and $\bar{\mathbf{B}}$.

To enhance dynamic feature modeling, Mamba [12] adopts an input-aware parameterization for \mathbf{B} , \mathbf{C} , and Δ . Similar to

the recursive formulation in Eq. (3), Mamba excels at propagating information through exceptionally long sequences, a capability that is pivotal for integrating global pixel information during restoration. However, unlike standard recurrent architectures, Mamba utilizes a hardware-aware parallel scan algorithm [12]. This approach inherits the parallel processing advantages of Eq. (3), significantly optimizing the efficiency of both training and inference.

B. Challenge of State Space Model

To extend one-dimensional SSMs to two-dimensional visual tasks, the vast majority of existing methods [11], [17], [20], [21], rely on the two-dimensional selective scanning mechanism (SS2D) [13] or its multi-directional variants. From an information-theoretic perspective, however, this mechanism suffers from a fundamental limitation. Natural images exhibit extremely high spatial redundancy at the pixel level, yet existing grid-based scanning forcibly flattens continuous two-dimensional visual signals into fixed-length one-dimensional sequences. This data-agnostic rigid scanning inevitably severs the inherent topological structure of objects. As illustrated in Fig. 1(a), physically adjacent regions are stretched to extreme distances after forced serialization, causing long-range dependency decay within excessively long and redundant sequences. Simultaneously, fixed-grid partitioning fragments originally coherent semantic regions, such as repetitive sky or water textures, into disconnected pieces, which readily induces semantic confusion.

To bridge this gap, we resort to the perceptual grouping theory in Gestalt psychology [22]. The human visual system naturally tends to aggregate pixels sharing similar color and texture into coherent entities. Motivated by this theory, we propose using superpixels as the input primitives of the SSM. Unlike naive grid-based patch partitioning, superpixel clustering is essentially a structure-aware information bottleneck:

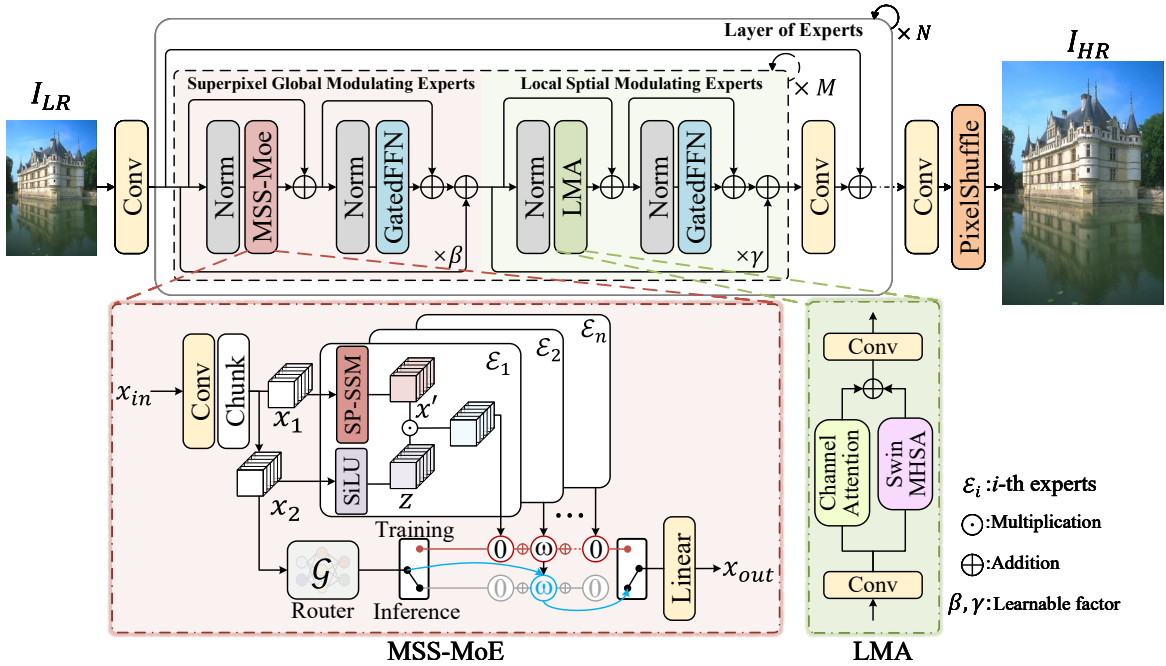


Fig. 3: Architecture of SP-MoMamba, built upon stacked Layers of Experts (LoEs) that hierarchically couple two complementary experts. Among all components, the superpixel-driven semantic scanning mechanism (SP-SSM) and expert design (MSS-MoE) are the central contribution, modeling semantic interaction and efficiency. As an auxiliary design, LSME employs Local Mixed Attention (LMA) to recover high-frequency details smoothed during global abstraction.

it filters out low-level local redundancy while maximally preserving the core semantic manifold of the image. Through this process, the low-level dense pixel sequence is elevated into a high-level, compact semantic token sequence. This not only substantially reduces the sequence length of the SSM, but also liberates it entirely from meaningless spatial exhaustion, enabling the model to focus on semantic interactions among global visual entities in a manner analogous to processing natural language tokens.

C. Visual Analysis of Semantic Preservation

To intuitively and quantitatively validate the superiority of our superpixel-based SSM in semantic preservation, we conduct an in-depth analysis of the model’s receptive field and information utilization patterns using Local Attribution Maps (LAM) and the Diffusion Index (DI) [43], as shown in Fig. 2. It can be clearly observed that when reconstructing the texture details of flying birds, the LAM responses of conventional methods (MambaIR [11] and MambaIRv2 [20]) exhibit pronounced fragmentation and spatial locality. This directly exposes a critical weakness of conventional one-dimensional rigid scanning: because the spatial structure is disrupted and the sequence is excessively long, the model loses long-range context and is forced to aggregate information from a very limited neighborhood for reconstruction. In contrast, the proposed SP-MoMamba exhibits a markedly different feature attribution pattern. Its LAM responses not only cover a substantially wider range, but more importantly, the highly activated regions are strongly structured and strictly conform to the true semantic boundaries of the multiple birds present

in the image. This indicates that the model successfully establishes a direct semantic channel that operates independently of physical spatial distance. When reconstructing the target region, SP-MoMamba precisely and adaptively aggregates information from all structurally similar regions across the image, namely the other birds, through global interactions among superpixel nodes, without being distracted by the background sky. This content-aware long-range aggregation capability is directly reflected in the DI score of 24.36. These results compellingly demonstrate that using superpixels as the bridge between visual signals and the SSM substantially alleviates the semantic fragmentation problem of Mamba-based models in visual tasks, achieving a coherent unification of global topology understanding and local detail reconstruction.

IV. METHODOLOGY

In this section, we present our proposed SP-MoMamba, as illustrated in Fig. 3. The complete architecture of our pipeline integrates N layers of experts (LoEs) and upsampling layers. Initially, a 3×3 convolutional operation is employed to extract shallow features from the input low-resolution image. These features are then processed through a series of LoEs to recover deep features. Each LoE consists of M paired sets of Superpixel Global Modulating Experts (SGME) and Local Spatial Modulating Experts (LSME), collaboratively enhancing feature restoration. SGME adopts a collaborative reconstruction method by integrating a multi-scale superpixels mixture of state space experts (MSS-MoE), maximizing the interaction of global information. LSME concentrates on refining local features through a localized mixed attention mechanism,

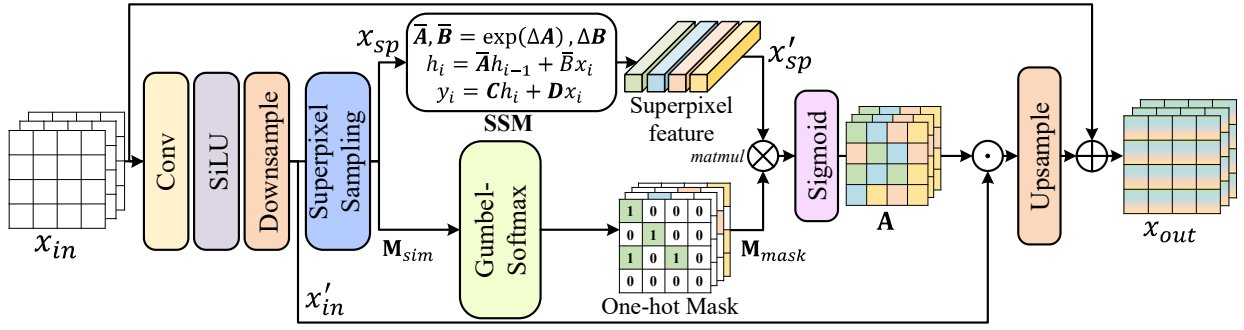


Fig. 4: Illustration of the superpixel-driven state space model (SP-SSM). One-hot mask should be $N \times M$, which is converted into a 3D matrix $(H \times W) \times M$ for ease of understanding in the figure.

which enhances overall performance. In addition, two residual connections with learnable scales β , and γ are introduced. Finally, the refined deep features are transformed into high-resolution images via a pixelshuffle and convolution.

A. Superpixel Global Modulating Experts

Unlike prior works [20], [21], [34], [35], which rely on substantial computational resources, we prioritize efficiency by constructing global similarity relationships based on interactions among the most relevant scale-specific superpixels. As shown in Fig. 3, we propose the MSS-MoE, which improves multi-scale modeling while keeping the dominant inference cost bounded by the selected top- k experts. MSS-MoE employs superpixel-driven state space models (SP-SSMs) at different scales to independently model global features across different resolutions. By leveraging the strengths of the mixture of experts scheme, it selectively integrates the resulting features, ensuring optimal global modeling within each LoE. Then, a Gated Feed-Forward Network (GatedFFN) [44] is utilized to aggregate contextual information from these global features.

1) *Multi-scale Superpixel Mixture of State Space Experts (MSS-MOE)*: As shown in Fig. 3, the output features from the last layer normalization serve as the input features x_{in} for this module. A Linear layer is first applied to increase the dimensionality of the feature channels, followed by a split along the channel dimension to yield two distinct features, x_1 and x_2 . Subsequently, we employ a SP-SSM module to derive the global attention feature x' from x_1 . Meanwhile, x_2 is processed through an activation function to obtain the gating feature z . Consequently, the formulation for each superpixel state space expert is expressed as follows:

$$\mathcal{E}_i(x_1, x_2, s) = x' \odot z = \text{SP-SSM}(x_1, s) \odot \sigma(x_2) \quad (7)$$

where $\text{SP-SSM}(\cdot)$ and $\sigma(\cdot)$ denote the SP-SSM module and the SiLU [45] activation function, respectively. The \odot denotes Hadamard product. The s represents the scale parameter of SP-SSM. We employ an SP-SSM to ensure robust modeling of global information while introducing a residual connection to prevent the loss of local information.

However, the SP-SSM operating at a fixed scale may fail to fully exploit all internal information, thereby limiting the model's expressive capacity. To address this, we propose an

ensemble approach that integrates superpixel state space experts across multiple scales s_i . A routing network searches the solution space to identify the optimal scale for the superpixel state space experts based on the input and network depth. The final output x_{out} of the MSS-MoE is formulated as follows:

$$x_{out} = \sum_i^n \mathcal{G}(x_2) \mathcal{E}_i(x_1, x_2, s_i) \quad (8)$$

where $\mathcal{G}(\cdot)$ and $\mathcal{E}(\cdot)$ denote the router function and the i -th expert function, respectively. The s_i represents the scale parameter of the i -th expert's SP-SSM module. Specifically, a router $\mathcal{G}(\cdot)$ is composed of a linear mapping and Softmax to map input features into weights of different superpixel state space experts. The sparsity inherent in the router function $\mathcal{G}(\cdot)$ optimizes computation by assigning greater weights to the top- k superpixel state space experts. During training, our method learns from all superpixel state space experts, while during inference, it utilizes only the selected top- k experts with higher routing weights for computation, thereby enhancing efficiency. Hence, the computational complexity of the inference process becomes independent of the total number of experts, further enhancing efficiency.

2) *Superpixel-driven State Space Model (SP-SSM)*: As shown in Fig. 4, given the input feature $x_{in} \in \mathbb{R}^{H \times W \times C}$, we use 3×3 convolution and SiLU activation function to map features. Then, these features are downsampled by a factor of s , and superpixel sampling is performed to obtain the corresponding M superpixel features $x_{sp} \in \mathbb{R}^{M \times C}$ and similarity matrix $\mathbf{M}_{sim} \in \mathbb{R}^{N \times M}$ (where $N = H \times W$). It is formulated as follows:

$$x_{sp}, \mathbf{M}_{sim} = \text{SPS}(\sigma(\text{Conv}(x_{in})) \downarrow_s) \quad (9)$$

where $\text{SPS}(\cdot)$ denotes the superpixel sampling operation. \downarrow_s represents the downsampling operation by a factor of s . Subsequently, a SSM is employed to perform global information modeling on the superpixel feature x_{sp} , yielding an enhanced superpixel feature $x'_{sp} \in \mathbb{R}^{M \times C}$. We use Gumbel-Softmax [46] to transform the similarity matrix \mathbf{M}_{sim} into a differentiable one-hot mask $\mathbf{M}_{mask} \in \mathbb{R}^{N \times M}$, while effectively maintaining stable superpixel to pixel propagation during the training process. Then, matrix multiplication followed by a

sigmoid function is utilized to derive the global attention feature $\mathbf{A} \in \mathbb{R}^{N \times C}$, as follows:

$$x'_{sp} = \text{SSM}(x_{sp}) \quad (10)$$

$$\mathbf{M}_{mask} = \text{Gumbel-Softmax}(\mathbf{M}_{sim}) \quad (11)$$

$$\mathbf{A} = \text{Sigmoid}(\mathbf{M}_{mask} \otimes x'_{sp}) \quad (12)$$

where $\text{Sigmoid}(\cdot)$ and \otimes denote sigmoid function and matrix multiplication. The final output of this module is obtained by multiplying the attention feature \mathbf{A} with x'_{in} , followed by the addition of the original transformed feature x_{in} , as follows:

$$x_{out} = (\mathbf{A} \odot x'_{in}) \uparrow_s + x_{in} \quad (13)$$

Since superpixels encapsulate comprehensive semantic information, the resulting output features effectively capture correlations among distinct semantics.

3) *Superpixel Sampling*: We follow the soft k -means-based superpixel algorithm in SSN [47] to perform superpixel sampling on images. Given input as $\mathbf{x} \in \mathbb{R}^{N \times C}$ (where $N = H \times W$), M superpixels $\mathbf{s} \in \mathbb{R}^{M \times C}$ and similarity matrix $\mathbf{M}_{sim} \in \mathbb{R}^{N \times M}$ are obtained through T iterations, maximizing their association with the corresponding pixels. Firstly, as shown in Fig. 5, we use average pooling to initialize superpixels \mathbf{s}^0 . Then, we conduct iterations using a similarity matrix that calculates the similarity between each pixel and superpixel. It can be formulated as follows:

$$\mathbf{M}_{sim}^t(i, j) = e^{-\|\mathbf{x}(i) - \mathbf{s}^{t-1}(j)\|_2^2} \quad (14)$$

Notably, superpixel sampling solely evaluates the similarity mapping between each pixel and its neighboring superpixels. This preserves the local coherence of superpixels, thereby enhancing computational efficiency. Subsequently, we can obtain the superpixel \mathbf{s}^t by computing a weighted sum of all pixels, defined as:

$$\mathbf{s}_j^t = \frac{1}{\mathbf{z}^t(j)} \sum_i \mathbf{M}_{sim}^t(i, j) \mathbf{x}(i) \quad (15)$$

where $\mathbf{z}^t(j) = \sum_i \mathbf{M}_{sim}^t(i, j)$ denotes the normalization term along the column. After T iterations, we can obtain the final similarity matrix \mathbf{M}_{sim}^T and superpixels \mathbf{s}^T . Using the similarity matrix, we can assign each pixel to its most similar superpixel, thus generating the corresponding mask, as depicted in Fig. 5. Therefore, with the superpixels and their respective masks, we can perform superpixel-based attention weighting on pixels across distinct regions. Our proposed SP-SSM utilizes this critical insight by employing a SSM to assign weights to superpixels, enabling weighted processing of semantic information across distinct regions.

B. Local Spatial Modulating Experts

After the proposed MSS-MoE primarily leverages superpixels to capture global semantic relationships, we enhance its capability by incorporating Local Spatial Modulation Experts (LSME) to strengthen the processing of local information. Given that MSS-MoE requires scanning only a limited number of superpixels, this property is insufficient for the modeling of local correlation. Consequently, we adopt a robust combination

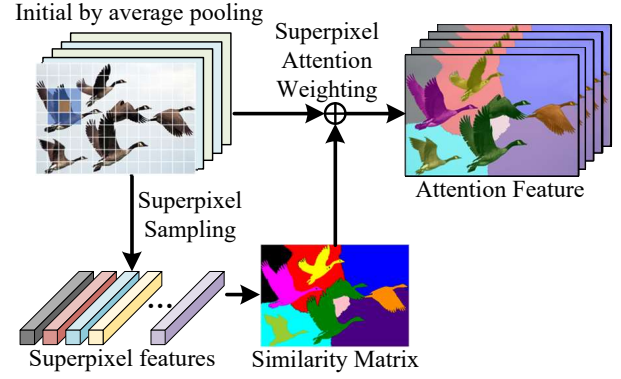


Fig. 5: Superpixel sampling of our method, which initializes the superpixel features by average pooling, and then generates the superpixel features and similarity matrix.

of shift window-based multi-head self-attention (SwinMHSA) and channel attention to construct a Local Mixed Attention Module (LMA), as depicted in Fig. 3. Channel attention recalibrates features across channels to emphasize salient local information; subsequently, SwinMHSA captures fine-grained spatial dependencies within local windows. GatedFFN then refines features by integrating global and local information, preserving prior semantics while enhancing detail capture, thus improving overall model performance.

V. EXPERIMENTS

A. Experimental Settings

1) *Datasets and Evaluation*: Following the previous SR methods [4], [39], we utilize two widely-used datasets, DIV2K [53] and Flickr2K [2] for training. We assess our method performance on five classical benchmark datasets for SR, Set5 [54], Set14 [55], BSD100 [56], Urban100 [57], and Manga109 [58]. We also quantify the effectiveness of our method using the PSNR and SSIM metrics on the Y-channel from the YCbCr color space.

2) *Implementation Details*: To thoroughly train the proposed model, we augment the training data by randomly cropping it into 64×64 patches and further augment it through random rotations, horizontal and vertical flips. Consistent with [59], we use the Adam [60] optimizer to minimize the L_1 norm between the SR output and the HR ground truth in both pixel and frequency domains across 500K iterations. The batch size is set to 32, with an initial learning rate of 1×10^{-3} which is halved at iterations [250K, 400K, 450K, 475K]. All experiments are implemented using the PyTorch framework and conducted on a single RTX 4090 GPU. We have designed two variants of the SP MoMamba model with different parameter configurations, including the our small model (SP-MoMamba-T) with 3 LoEs and 2 SGMEs and LSMEs. Additionally, our base model (SP-MoMamba-B) with 4 LoEs and 2 SGMEs and LSMEs. The channel dimension of SP-MoMamba-B is 48. For all MSS-MoE modules, we configure three experts with downsampling factors of [1, 2, 4]. To further improve the performance of SP-MoMamba-B, we adopt the self-ensemble strategy [2] to SP-MoMamba-B

TABLE I: Comparison to ultra-lightweight SR models. PSNR (dB \uparrow) and SSIM (\uparrow) metrics are reported on the Y-channel. **Best** and **second best** performances are highlighted. GMACs (G) are computed by upscaling to a 1280×720 HR image.

Scale	Model	Params \downarrow	GMACs \downarrow	Set5		Set14		BSD100		Urban100		Manga109		
				PSNR \uparrow	SSIM \uparrow	PSNR \uparrow	SSIM \uparrow	PSNR \uparrow	SSIM \uparrow	PSNR \uparrow	SSIM \uparrow	PSNR \uparrow	SSIM \uparrow	
$\times 2$	PAN [48]	261K	71	38.00	0.9605	33.59	0.9181	32.18	0.8997	32.01	0.9273	38.70	0.9773	
	DRSAN [49]	370K	86	37.99	0.9606	33.57	0.9177	32.16	0.8999	32.10	0.9279	—	—	
	SAFMN [30]	228K	52	38.00	0.9605	33.54	0.9177	32.16	0.8995	31.84	0.9266	38.71	0.9771	
	FECAN-tiny [50]	107K	24	38.00	0.9605	33.52	0.9172	32.14	0.8993	31.86	0.9252	38.76	0.9772	
	SeemoRe-T [39]	220K	45	38.06	0.9608	33.65	0.9186	32.23	0.9004	32.22	0.9286	39.01	0.9777	
	SRConvNet [51]	387K	74	38.00	0.9605	33.58	0.9186	32.16	0.8995	32.05	0.9272	38.87	0.9774	
	CFSR [52]	291K	63	38.07	0.9607	33.74	0.9192	32.24	0.9005	32.28	0.9300	39.00	0.9778	
	SP-MoMamba-T (ours)	259K	85	38.16	0.9612	33.81	0.9199	32.29	0.9011	32.48	0.9312	39.76	0.9820	
	$\times 3$	PAN [48]	261K	39	34.40	0.9271	30.36	0.8423	29.11	0.8050	28.11	0.8511	33.61	0.9448
DRSAN [49]		410K	43	34.41	0.9272	30.27	0.8413	29.08	0.8056	28.19	0.8529	—	—	
SAFMN [30]		233K	23	34.34	0.9270	30.33	0.8418	29.08	0.8048	27.95	0.8474	33.52	0.9437	
SeemoRe-T [39]		225K	20	34.46	0.9276	30.44	0.8445	29.15	0.8063	28.27	0.8538	33.92	0.9460	
SRConvNet [51]		387K	33	34.40	0.9272	30.30	0.8416	29.07	0.8500	28.04	0.8474	33.56	0.9443	
CFSR [52]		298K	29	34.50	0.9279	30.44	0.8437	29.16	0.8066	28.29	0.8553	33.86	0.9462	
SP-MoMamba-T (ours)		264K	37	34.53	0.9284	30.50	0.8448	29.19	0.8080	28.43	0.8572	34.16	0.9504	
$\times 4$		PAN [48]	272K	28	32.13	0.8948	28.61	0.7822	27.59	0.7363	26.11	0.7854	30.51	0.9095
		DRSAN [49]	410K	31	32.15	0.8935	28.54	0.7813	27.54	0.7364	26.06	0.7858	—	—
	SAFMN [30]	240K	14	32.18	0.8948	28.60	0.7813	27.58	0.7359	25.97	0.7809	30.43	0.9063	
	FECAN-tiny [50]	121K	7	32.08	0.8935	28.58	0.7809	27.57	0.7354	25.96	0.7801	30.33	0.9049	
	SeemoRe-T [39]	232K	12	32.31	0.8965	28.72	0.7840	27.65	0.7384	26.23	0.7883	30.82	0.9107	
	SRConvNet [51]	382K	22	32.18	0.8951	28.61	0.7359	27.57	0.7359	26.06	0.7845	30.35	0.9075	
	CFSR [52]	307K	18	32.33	0.8964	28.73	0.7842	27.63	0.7381	26.21	0.7897	30.72	0.9111	
	SP-MoMamba-T (ours)	271K	22	32.35	0.8970	28.77	0.7850	27.69	0.7398	26.40	0.7939	31.01	0.9160	

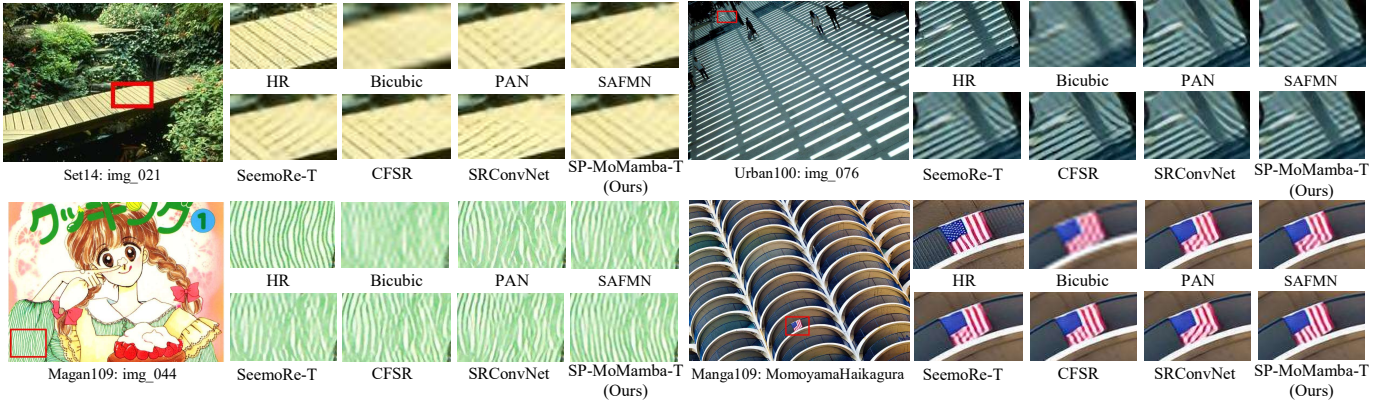


Fig. 6: Qualitative comparison of our SP-MoMamba-T with state-of-the-art ultra-lightweight methods on $4\times$ SR. (Zoom in for the best view)

and denote the self-ensemble version as SP-MoMamba-B+. Further details are provided in Supplementary Material.

B. Comparisons with Ultra-lightweight SR Methods

1) *Quantitative comparison:* Following prior work [39], we define ultra-lightweight models as those operating under a sub-500K parameter budget. To thoroughly evaluate the performance, we compare the proposed SP-MoMamba-T against state-of-the-art ultra-lightweight SR models, including CARN-M [29], PAN [48], DRSAN [49], SAFMN [30], FECAN-tiny [50], SeemoRe-T [39], SRConvNet [51], and CFSR [52]. As reported in Table I, SP-MoMamba-T consistently yields the highest PSNR and SSIM scores across all scaling factors ($\times 2$, $\times 3$, and $\times 4$) on all five benchmark datasets. Notably, our method demonstrates significant advantages on datasets containing rich high-frequency details, such as Urban100 [57] and Manga109 [58]. For example, under the $\times 4$ SR setting on the Urban100 dataset, SP-MoMamba-T achieves a PSNR of 26.40 dB, substantially outperforming recent highly competitive models like SeemoRe-T (26.23 dB) and CFSR (26.21 dB). Furthermore, despite achieving state-of-

the-art restoration quality, our model maintains exceptional computational efficiency. In the $\times 4$ setting, SP-MoMamba-T requires only 271K parameters and 22G GMACs. This excellent performance-efficiency trade-off indicates that our architectural design effectively enhances feature representation capacity without introducing a heavy computational burden.

2) *Qualitative comparison:* To further demonstrate the visual superiority of our proposed SP-MoMamba-T under the ultra-lightweight setting, we provide qualitative comparisons for $\times 4$ SR in Fig. 6. It can be consistently observed that our method exhibits exceptional capability in recovering high-frequency details and maintaining structural coherence, whereas existing efficient models frequently struggle with severe blurring or aliasing artifacts. Specifically, in the complex striped patterns of the green dress (img_044) and the fine-grained details of the small flag (MomoyamaHaikagura), most baselines fail to resolve the individual lines, producing smudged textures or structural artifacts with incorrect orientations. In contrast, SP-MoMamba-T faithfully reconstructs clear, continuous stripes that closely match the ground-truth (HR) images. Similarly, for the slanted geometric shadows

TABLE II: Comparison to standard lightweight SR models. PSNR (dB \uparrow) and SSIM (\uparrow) metrics are reported on the Y-channel. **Best** and **second best** performances are highlighted. GMACs (G) are computed by upscaling to a 1280×720 HR image. * denote retraining based on equivalent experimental configuration.

Scale	Model	Params \downarrow	GMACs \downarrow	Set5		Set14		BSD100		Urban100		Manga109		
				PSNR \uparrow	SSIM \uparrow	PSNR \uparrow	SSIM \uparrow	PSNR \uparrow	SSIM \uparrow	PSNR \uparrow	SSIM \uparrow	PSNR \uparrow	SSIM \uparrow	
$\times 2$	SwinIR-Light	910K	244	38.14	0.9611	33.86	0.9206	32.31	0.9012	32.76	0.9340	39.12	0.9783	
	SRFormer-Light	853K	236	38.23	0.9613	33.94	0.9209	32.36	0.9019	32.91	0.9353	39.28	0.9785	
	SPIN	497K	320	38.20	0.9615	33.90	0.9215	32.31	0.9015	32.79	0.9340	39.18	0.9784	
	CAMixerSR	746K	205	38.23	0.9613	34.00	0.9214	32.34	0.9016	32.95	0.9340	39.32	0.9781	
	FECAN-light*	732K	162	38.22	0.9614	34.01	0.9216	32.35	0.9017	32.89	0.9347	39.47	0.9784	
	Freqformer*	870K	229	38.26	0.9615	34.02	0.9217	32.34	0.9018	32.94	0.9353	39.47	0.9789	
	MambaIR-light	905K	334	38.13	0.9610	33.95	0.9208	32.31	0.9013	32.85	0.9349	39.20	0.9782	
	SeemoRe-L	931K	197	38.27	0.9616	34.01	0.9210	32.35	0.9018	32.87	0.9344	39.49	0.9790	
	CRAFT	738K	197	38.23	0.9615	33.92	0.9211	32.33	0.9016	32.86	0.9343	39.39	0.9786	
	MambaIRv2-light	774K	286	38.26	0.9615	<u>34.09</u>	0.9221	32.36	0.9019	33.26	0.9378	39.35	0.9785	
	DMNet	572K	115	38.23	0.9613	33.95	0.9209	32.31	0.9015	32.84	0.9347	39.39	0.9766	
	SP-MoMamba-B (ours)	543K	170	<u>38.27</u>	<u>0.9616</u>	34.04	<u>0.9219</u>	<u>32.38</u>	<u>0.9022</u>	32.99	0.9357	40.18	<u>0.9827</u>	
SP-MoMamba-B+ (ours)	543K	170	38.31	0.9617	34.12	0.9221	32.41	0.9025	<u>33.17</u>	<u>0.9371</u>	40.35	0.9830		
$\times 3$	SwinIR-Light	918K	111	34.62	0.9289	30.54	0.8463	29.20	0.8082	28.66	0.8624	33.98	0.9478	
	SRFormer-Light	861K	105	34.67	0.9296	30.57	0.8469	29.26	0.8099	28.81	0.8655	34.19	0.9489	
	SPIN	569K	176	34.65	0.9293	30.57	0.8464	29.23	0.8089	28.71	0.8627	34.24	0.9489	
	MambaIR-light	913K	149	34.63	0.9288	30.54	0.8459	29.23	0.8084	28.70	0.8631	34.12	0.9479	
	SeemoRe-L	959K	87	34.70	0.9297	30.60	0.8469	29.29	0.8101	28.86	0.8653	34.53	0.9496	
	CRAFT	744K	88	34.71	0.9295	30.61	0.8469	29.24	0.8093	28.77	0.8635	34.29	0.9491	
	MambaIRv2-light	781K	127	34.71	0.9297	<u>30.68</u>	<u>0.8483</u>	29.26	0.8098	29.01	0.8689	34.41	0.9497	
	DMNet	579K	52	34.71	0.9295	30.57	0.8459	29.26	0.8093	28.80	0.8640	34.33	0.9488	
	SP-MoMamba-B (ours)	550K	75	<u>34.71</u>	<u>0.9297</u>	30.65	0.8478	<u>29.29</u>	<u>0.8104</u>	28.84	0.8652	34.67	<u>0.9530</u>	
	SP-MoMamba-B+ (ours)	550K	75	34.75	0.9302	30.72	0.8488	29.32	0.8111	28.96	0.8669	34.94	0.9543	
	$\times 4$	SwinIR-Light	930K	64	32.44	0.8976	28.77	0.7858	27.69	0.7406	26.47	0.7980	30.91	0.9151
		SRFormer-Light	873K	63	32.51	0.8988	28.82	0.7872	27.73	0.7422	26.67	0.8032	31.17	0.9165
SPIN		555K	90	32.48	0.8983	28.80	0.7862	27.70	0.7415	26.55	0.7998	30.98	0.9156	
CAMixerSR		765K	54	32.51	0.8988	28.82	0.7870	27.72	0.7416	26.63	0.8012	31.18	0.9166	
FECAN-light*		749K	42	32.53	0.8990	28.89	0.7879	27.75	0.7421	26.78	0.8049	31.47	0.9181	
FreqFormer*		889K	55	32.54	0.8991	28.89	0.7879	27.76	0.7425	26.73	0.8023	31.36	0.9178	
MambaIR-light		924K	85	32.42	0.8977	28.74	0.7847	27.68	0.7400	26.52	0.7983	30.94	0.9135	
SeemoRe-L		969K	50	32.51	0.8990	28.92	0.7881	27.77	<u>0.7428</u>	26.79	0.8046	31.48	0.9181	
CRAFT		753K	52	32.52	0.8989	28.85	0.7872	27.72	0.7418	26.56	0.7995	31.18	0.9168	
MambaIRv2-light		790K	76	32.51	0.8992	28.84	0.7878	27.75	0.7425	<u>26.82</u>	0.8079	31.24	0.9182	
DMNet		588K	30	32.51	0.8987	28.84	0.7866	27.73	0.7410	26.58	0.7991	31.14	0.9150	
SP-MoMamba-B (ours)		559K	46	<u>32.56</u>	<u>0.8992</u>	<u>28.93</u>	<u>0.7885</u>	<u>27.78</u>	0.7426	26.76	0.8030	<u>31.51</u>	<u>0.9210</u>	
SP-MoMamba-B+ (ours)	559K	46	32.63	0.9003	28.98	0.7897	27.81	0.7434	26.86	<u>0.8050</u>	31.75	0.9232		

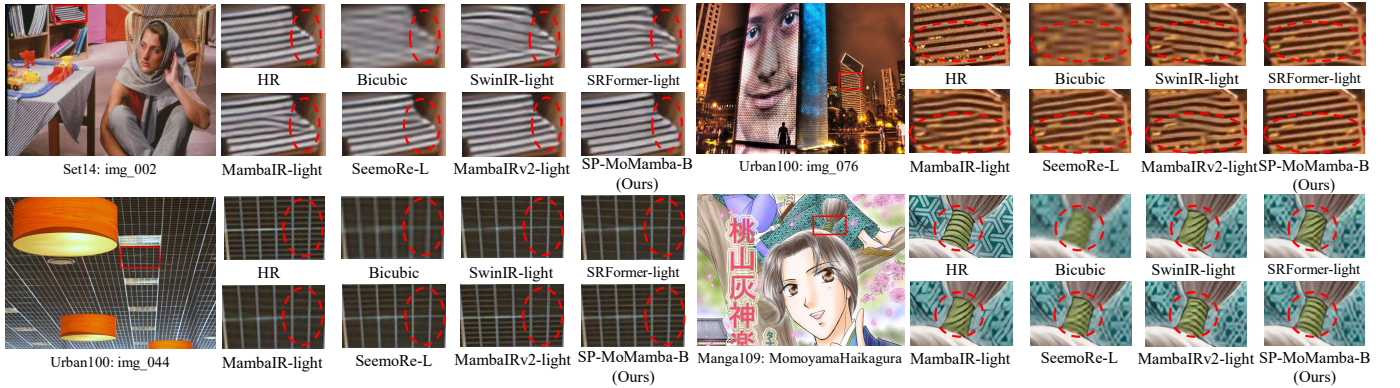


Fig. 7: Qualitative comparison of our SP-MoMamba-B with state-of-the-art methods on $4 \times$ SR. (Zoom in for the best view)

in img_076, competing methods suffer from heavily distorted lines and blurred edges, whereas our approach successfully alleviates these structural distortions to recover sharp boundaries and accurate line directions. These compelling visual results corroborate that SP-MoMamba-T effectively captures critical structural information and fine textures, achieving outstanding restoration quality even under extreme parameter constraints.

C. Comparisons with lightweight SR Methods

1) *Quantitative comparison:* To further evaluate our approach under the standard lightweight setting, we com-

pare the proposed SP-MoMamba-B and its enhanced variant SP-MoMamba-B+ against a wide range of state-of-the-art lightweight SR networks. The competitors include representative CNN-based models (SPIN [34], CAMixerSR [62], FECAN-light [50], SeemoRe-L [39], CRAFT [63], and DMNet [64]), Transformer-based architectures (e.g., SwinIR-Light [4], SRFormer-Light [6]), and recent advanced Mamba-based methods (e.g., MambaIR-light [11], MambaIRv2-light [20]). As summarized in the provided quantitative Table II, our models demonstrate an extraordinary performance-parameter trade-off. Impressively, SP-MoMamba-B utilizes significantly fewer parameters (550K) compared to mainstream lightweight

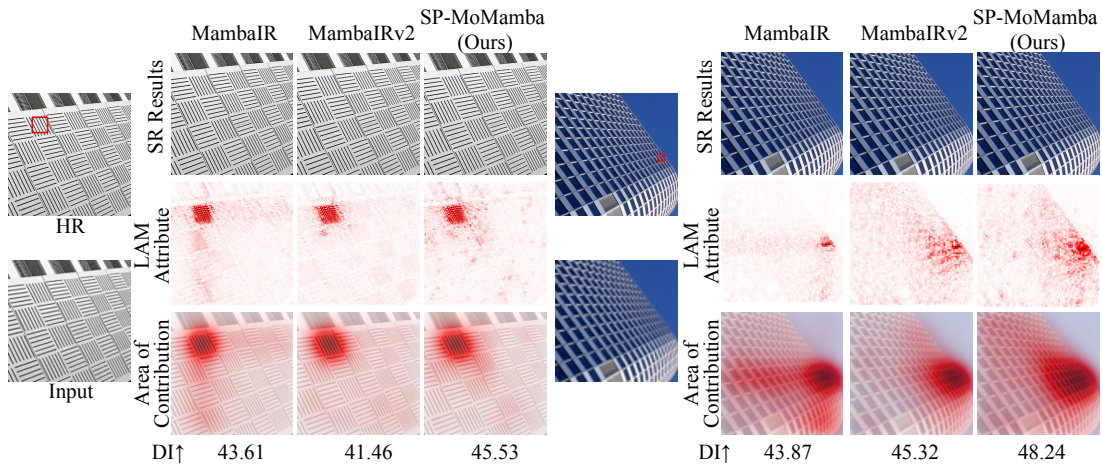


Fig. 8: Visual comparison of Local Attribution Maps (LAM) [43] and Diffusion Indices (DI). The red dot indicates the target pixel selected for analysis. Our SP-MoMamba exhibits a significantly broader feature activation range and secures the highest DI scores compared to MambaIR [11] and MambaIRv2 [20]. These results validate its superior capability to capture long-range dependencies and utilize global structural information for accurate texture reconstruction.

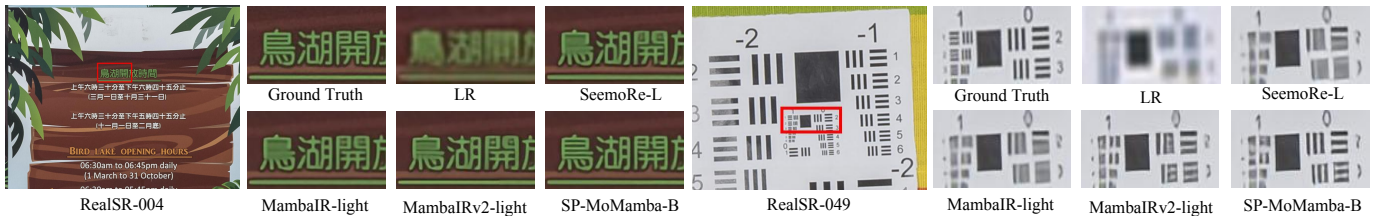


Fig. 9: Qualitative comparisons with existing efficient SR methods on the real-world test set RealSRv3 [61]. (Zoom in for the best view)

models, which typically require around 800K to 950K parameters (e.g., 897K for SwinIR-Light and 969K for SeemoRe-L in the $\times 4$ task). Despite this remarkable reduction in model capacity, SP-MoMamba-B consistently achieves competitive or superior PSNR and SSIM scores across all benchmark datasets. Furthermore, our enhanced SP-MoMamba-B+ establishes new state-of-the-art records. For instance, on the challenging Manga109 dataset for $\times 4$ upscaling, SP-MoMamba-B+ achieves a remarkable PSNR of 31.75 dB, significantly surpassing the highly competitive SeemoRe-L (31.48 dB) and MambaIRv2-light (31.24 dB). These results compellingly validate that our architecture is highly parameter-efficient while maintaining top-tier representation capabilities.

2) *Qualitative comparison:* We provide visual comparisons of our SP-MoMamba-B against other prominent lightweight models in Fig. 7. Consistent with the quantitative metrics, our method effectively restores highly structured patterns and intricate high-frequency textures without introducing aliasing artifacts. Specifically, in `img_044` from Urban100, competing methods such as SwinIR-Light and SeemoRe-L fail to correctly reconstruct the intersecting ceiling grids, resulting in severe blurring and disconnected lines. In contrast, SP-MoMamba-B faithfully recovers continuous and sharp structural grids. Similarly, for the dense horizontal lines on the building facade in `img_076` (Urban100), baseline models suffer from noticeable structural distortions and blended edges.

Our approach successfully mitigates these artifacts, maintaining strict structural fidelity. Furthermore, in the complex braided texture shown in `MomoyamaHaikagura` (Manga109), other methods produce smudged or diagonally distorted patterns, whereas SP-MoMamba-B precisely resolves the tightly packed, fine-grained bands with accurate orientations. These superior visual results confirm the effectiveness of our model in capturing long-range dependencies and accurately reconstructing complex geometric details.

To further investigate this global modeling capability, we analyze the Local Attribution Map (LAM) [43] and Diffusion Index (DI) results, as shown in Fig. 8. While MambaIR and MambaIRv2 display localized activation areas and struggle to connect spatially separated repeating textures, SP-MoMamba demonstrates a much wider area of contribution. It effectively leverages information from similar structures across the image to aid in restoration. This expanded receptive field is quantitatively supported by higher DI scores; for example, our method achieves DI scores of 45.53 and 48.24 on the two test images, consistently outperforming the baseline models. These results prove that our superpixel-based design successfully overcomes the local limitations of standard 1D scanning to capture true long-range dependencies.

TABLE III: Quantitative evaluation of our method and existing lightweight SR methods on a real-world test set.

Scale	Methods	Params	GMACs	RealSRv3 [61]
				PSNR \uparrow /SSIM \uparrow /LPIPS \downarrow
$\times 4$	SwinIR-light [4]	930K	64G	29.18/0.8278/0.2756
	MambaIR [11]	924K	85G	29.22/0.8286/0.2748
	SeemoRe-L [39]	715K	50G	29.24/0.8293/0.2764
	MambaIRv2 [20]	790K	76G	29.27/0.8295/0.2738
	SP-MoMamba-B (Ours)	559K	46G	29.31/0.8312/0.2711

D. Evaluation on Real-World Super-Resolution

To evaluate the practical applicability of our method, we conduct experiments on the real-world dataset, RealSRv3 [61], for $\times 4$ upscaling. As presented in Table III, SP-MoMamba-B consistently outperforms recent state-of-the-art lightweight models, including SwinIR-light, MambaIR, SeemoRe-L, and MambaIRv2. Specifically, our model achieves the highest PSNR (29.31 dB), SSIM (0.8312), and the lowest LPIPS (0.2711). Notably, it accomplishes best performance while maintaining the lowest computational footprint among the compared models, requiring only 559K parameters and 46G GMACs.

Consistent with these quantitative metrics, the qualitative comparisons in Fig. 9 further demonstrate our model’s robustness in real-world scenarios. For instance, in image RealSR-004, baseline methods struggle to reconstruct the complex Chinese characters, producing blurry and illegible text. In contrast, SP-MoMamba-B effectively recovers sharp and distinct strokes. Similarly, in the resolution test chart (RealSR-049), where competing models suffer from severe aliasing and blended lines, our method successfully restores the dense, tightly packed parallel lines with clean edges. These results confirm that SP-MoMamba provides an optimal balance between visual restoration quality and computational efficiency for practical applications.

E. Comparison of Model Efficiency

To comprehensively assess the practical applicability of our proposed methods, we evaluate their inference time and GPU memory consumption against recent state-of-the-art efficient SR models. As detailed in Table IV and illustrated in Fig. 10, these evaluations are conducted by generating 720p high-resolution (HR) images for the $\times 4$ upscaling task on the Manga109 dataset. Our models demonstrate a highly favorable trade-off between restoration performance and computational cost. Specifically, SP-MoMamba-T achieves the lowest inference latency (0.084s) and maintains the most compact memory footprint (4258.1 MB) among all compared methods, while still delivering competitive PSNR scores that surpass heavier models like SwinIR-Light and SPIN. Furthermore, our SP-MoMamba-B version establishes a state-of-the-art PSNR of 31.51 dB while remaining highly efficient. Compared to recent computationally expensive models such as Mambairv2-Light and CATANet, SP-MoMamba-B reduces inference time by over 70% and consumes substantially less GPU memory (6572.9 MB vs. 13652.3 MB and 21962.0 MB, respectively). Notably, when compared to SeemoRe-L—a strong baseline with fast inference—SP-MoMamba-B not only yields better

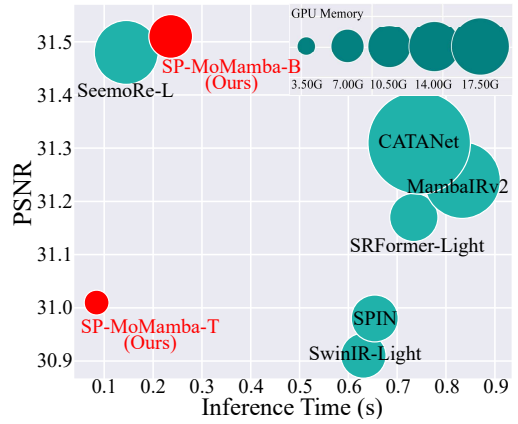


Fig. 10: Comparison between performance vs Inference times and GPU Memory on Manga109 $\times 4$ dataset. Inference times and GPU Memory are calculated on 720p HR image.

TABLE IV: Comparison between performance vs Inference times and GPU Memory on Manga109 $\times 4$ dataset.

Method	Time (s)	GPU Memory	PSNR
SwinIR-Light	0.631	6802.7	30.91
SRFormer-Light	0.734	7319.4	31.17
SPIN	0.654	7083	30.98
Mambairv2-Light	0.833	13652.3	31.24
CATANet	0.745	21962	31.31
SeemoRe-L	0.145	10464.7	31.48
SP-MoMamba-T	0.084	4258.1	31.01
SP-MoMamba-B	0.236	6572.9	31.51

restoration quality but also requires approximately 37% less GPU memory (6572.9 MB vs. 10464.7 MB). As indicated by the superior performance-to-cost positioning of our models in Fig. 10, our architecture effectively overcomes conventional efficiency limitations, proving to be highly practical for resource-constrained real-world applications.

F. Ablation Study

We devise a set of ablation studies to evaluate the contribution and efficacy of each proposed module. All experiments are conducted on the $\times 4$ SP-MoMamba-T setting.

1) *Macro Architecture*: As shown in Table V, we assess the effectiveness of our proposed key architectural components by comparing them against a baseline model composed solely of residual blocks. The progressive incorporation of these modules into the baseline framework yields significant and consistent enhancements in restoration performance. Specifically, the introduction of the State Space Model (SSM) and Superpixel Sampling (SPS) lays a solid foundation. Notably, SPS not only effectively reduces the computational cost (dropping GMACs from 18.7 to 16.7) but simultaneously boosts performance (e.g., increasing PSNR from 25.64 dB to 25.86 dB on Urban100), rather than merely maintaining it.

Furthermore, the addition of the Mixture-of-Experts (MoE) strategy and Local Mixed Attention (LMA) independently augments the model’s capability to capture complex features. To further elucidate the synergy of these mechanisms, we track the training dynamics as illustrated in the PSNR curves (Fig. 11(a)). The progression clearly demonstrates that the unified

TABLE V: Ablation on key components of SP-MoMamba. We show PSNR results for $\times 4$ upscaling.

Method	SGME			LSGE LMA	FFN GatedFFN	Performance			
	SSM	SPS	MoE			Params	GMACs	BSD100	Urban100
Baseline	-	-	-	-	-	189K	8.4	27.42	25.55
SP-MoMamba-T	✓	-	-	-	-	230K	18.7	27.48	25.64
	✓	✓	-	-	-	197K	16.7	27.54	25.86
	✓	✓	✓	-	-	242K	16.9	27.59	26.07
	-	-	-	✓	✓	211K	16.6	27.61	26.14
	✓	✓	✓	-	✓	261K	19.8	27.63	26.14
	✓	✓	✓	✓	✓	272K	22	27.69	26.40

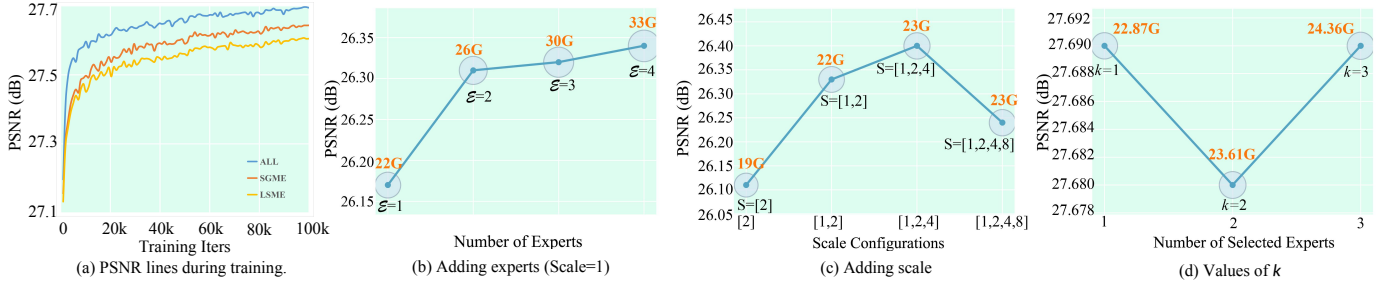


Fig. 11: Ablation studies of our SP-MoMamba-T at scale factors of $\times 4$ on BSD100 [56] test set. (a) represents ablation experiments of different key modules SGME and LSME. (b) and (c) are ablation experiments with different numbers of experts and scale factors, respectively. (d) is the ablation experiment with a value of k on MSS-MoA. \mathcal{E} and k respectively represent the number of experts and the number of selected experts.

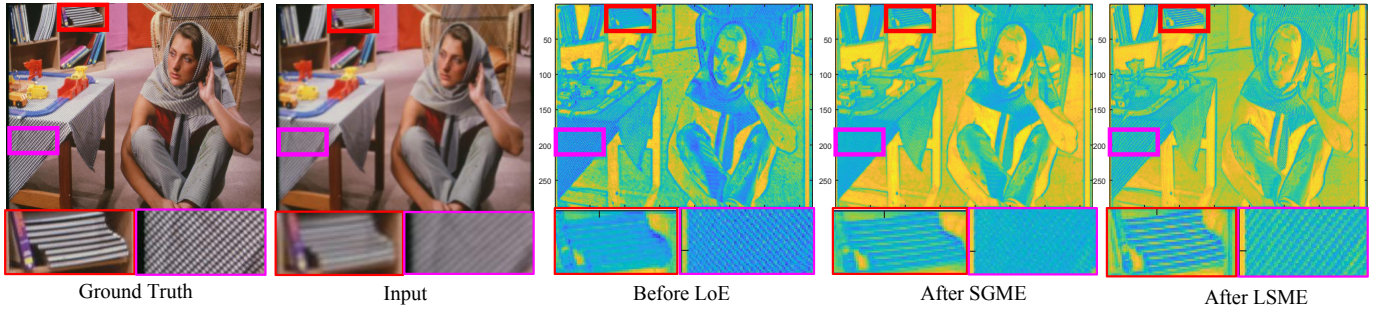


Fig. 12: Visualizations of feature maps before and after applying the proposed SGME and LSME modules, demonstrating enhanced activation sharpness through SGME and refined representations via LSME. (Zoom in for the best view)

macro architecture (“ALL”) achieves significantly faster convergence in the early stages and reaches a higher final PSNR peak compared to relying solely on individual specialized components (e.g., SGME or LSME) throughout the 100k training iterations.

Ultimately, the inclusion of the Gated Feed-Forward Network (GatedFFN) alongside these components leads to the optimal configuration (SP-MoMamba-T). This complete integration augments the baseline by 0.27 dB on BSD100 (27.42 dB to 27.69 dB) and an impressive 0.85 dB on Urban100 (25.55 dB to 26.40 dB). Although the overall parameter count increases moderately with the integration of all modules, these substantial performance gains compellingly validate the effectiveness and mutually beneficial synergy of each proposed component within the macro architecture.

To further demonstrate the effectiveness of the proposed SGME and LSME modules, we visualize the feature maps before and after they pass through the Layer of Experts (LoE), as shown in Fig. 12. This comparison clearly shows the benefits of using MSS-MoE within the SGME module to extract global

information, alongside the combination of Swin MHSA and CA in the LSME module to refine local details. Specifically, as highlighted by the red boxes, global structural textures are noticeably sharpened by the SGME module and then further detailed in the LSME stage. Furthermore, as indicated by the purple boxes, fine textures that might be smoothed over during the SGME filtering process are successfully recovered and added back in the LSME stage. This confirms that the two modules work together seamlessly to build a more complete and accurate feature representation.

2) *Design choices of MSS-MoE.*: We systematically explore the architectural configurations of the MSS-MoE module by varying the number of experts (\mathcal{E}) and their corresponding spatial scale factors (S). To determine the optimal routing strategy and scale distribution, we evaluate two distinct configuration scenarios for the $\times 4$ upscaling task on the BSD100 dataset.

The first scenario uniformly increases the number of experts at a single scale ($S = 1$), as depicted in Fig. 11(b). While adding experts steadily improves the PSNR, it introduces a severe computational burden, escalating the cost to 33G GMACs

TABLE VI: Superpixel sampling method. We compared the performance impact of different superpixel sampling method separately.

Method	Params	GMACs	BSD100	Urban100
w SLIC [65]	271K	26	27.51	26.03
w STA [66]	460K	38	27.72	26.49
w SSN (Ours)	271K	22	27.69	26.30

TABLE VII: Analysis of the impact of the number of superpixels on the performance of MSS-MoE.

Method	experts	Num superpixels	GMACs	BSD100	Urban100
SP-MoMamba-T	3	[64,64,64]	22	27.69	26.40
	3	[16,32,64]	21	27.65	26.28
	3	[32,64,128]	39	27.66	26.30

when $\mathcal{E} = 4$. Conversely, the second scenario incorporates experts across varying spatial scales (Fig. 11(c)). Notably, employing a multi-scale configuration of $S = [1, 2, 4]$ achieves a superior peak performance (26.40 dB) with only a modest computational cost of 23G GMACs, completely outperforming the uniform-scale method. However, expanding the scales further to $S = [1, 2, 4, 8]$ leads to a noticeable performance degradation (dropping to 26.24 dB). Based on these empirical observations, we assert that downsampling beyond a factor of 4 incurs a substantial loss of structural semantics, which introduces artifacts into the network and limits restoration quality. Consequently, we adopt the $S = [1, 2, 4]$ configuration as our optimal multi-scale expert baseline.

Furthermore, we analyze the impact of the routing parameter k , which dictates the number of selected experts per token, as shown in Fig. 11(d). The results clearly demonstrate that increasing k from 1 to 3 consistently increases the computational overhead (from 22.87G to 24.36G GMACs) without providing any PSNR benefits; in fact, the performance slightly dips at $k = 2$. Therefore, we decisively select $k = 1$ as the optimal setting to achieve the best performance with minimal architectural complexity. Ultimately, these comprehensive analyses indicate that our routing mechanism effectively leverages complementary semantic information across diverse scales. By dynamically assigning the single most appropriate expert via the router, the model significantly enhances its capacity for detailed, high-fidelity image reconstruction while maintaining strict computational efficiency.

3) *Micro-Architectural Design Choices*: To justify the specific internal configurations of our proposed modules, we conduct a series of micro-architectural ablation studies, as detailed in Tables VII, VI, VIII and Fig. 13.

Design choices of SP-SSM. We first investigate the design choices underlying the superpixel mechanism. Table VI compares our proposed SSN sampling method against established algorithms, namely SLIC [65] and STA [66]. Although some alternatives may obtain slightly higher scores in individual settings, our method offers a more favorable balance between reconstruction quality and computational cost. For example, The STA method achieved a PSNR of 27.72, but GMACs and Params reached 38 and 460K, respectively. Conversely, our SSN method strikes a superior balance, significantly outperforming SLIC while maintaining a highly efficient footprint

Aggregation method	Urban100	Manga109
(a)	32.11	38.96
(b)	32.15	38.99
(c)	32.17	38.97
(d)	32.22	39.01

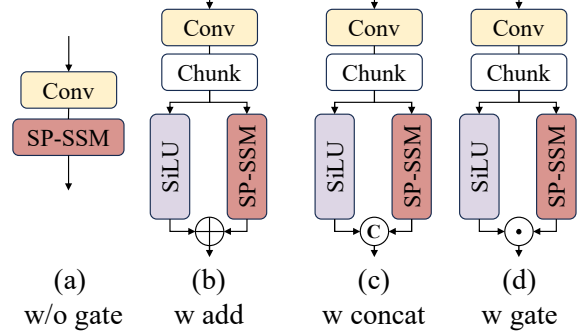


Fig. 13: Analysis of gating mechanism on SP-SSM. We provide further insights in the design decisions of our SP-MoMamba-T framework for $\times 2$ upscaling.

TABLE VIII: Ablation on the Local Mixed Attention (LMA) mechanism. We show results for $\times 4$ upscaling.

Method	Params	GMACs	BSD100	Urban100
Swin MHSA	224K	20	27.67	26.28
CA	240K	13	27.65	26.22
LMA	271K	22	27.69	26.40

of 271K parameters and 22G GMACs.

Building upon this, Table VII explores the impact of varying the number of superpixels within the MSS-MoE. An asymmetric configuration of [16, 32, 64] yields sub-optimal performance, whereas an excessive allocation of [32, 64, 128] substantially escalates the computational cost to 39G without delivering commensurate performance gains. Consequently, the uniform allocation of [64, 64, 64] superpixels is adopted, as it provides the optimal trade-off between restoration accuracy (26.40 dB on Urban100) and computational efficiency.

Finally, Fig. 13 evaluates the gating mechanism within the SP-SSM. Relying on a trivial addition operation (“w add”) yields merely marginal improvements. In contrast, integrating the dedicated gating mechanism significantly refines the selection of informative features, elevating the performance to 32.22 dB on Urban100 and 39.01 dB on Manga109 for $\times 2$ upscaling.

Feature Refinement and Modulation. Furthermore, we analyze the components designed for local feature enhancement and state space modulation. Table VIII validates the Local Mixed Attention (LMA) mechanism. Compared to conventional Swin MHSA and Channel Attention (CA), LMA demonstrates stronger representational capabilities, achieving the highest PSNR of 26.40 dB on Urban100. Although its parameter count is slightly higher than CA, the substantial gain in high-frequency detail recovery justifies its adoption.

G. Discussion on Experts

The decision-making process of the router across different residual groups is illustrated in Fig. 14(a). Notably, the net-

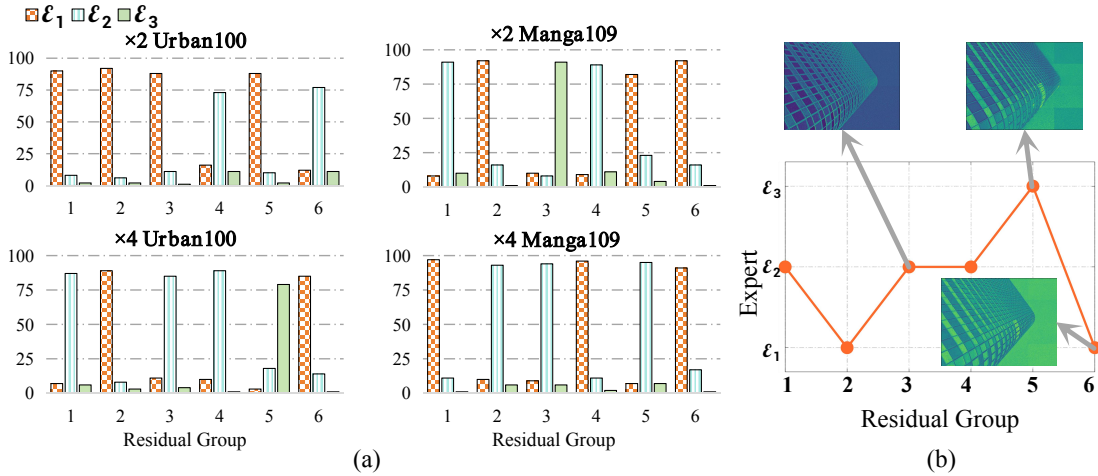


Fig. 14: Expert routing analysis. (a) We plot the decisions made by the routing function for SP-MoMamba-T over the depth of the network. (b) We visualize the expert output features of SP-MoMamba-T at different scales and depth for $\times 4$ SR given example images from Urban100.

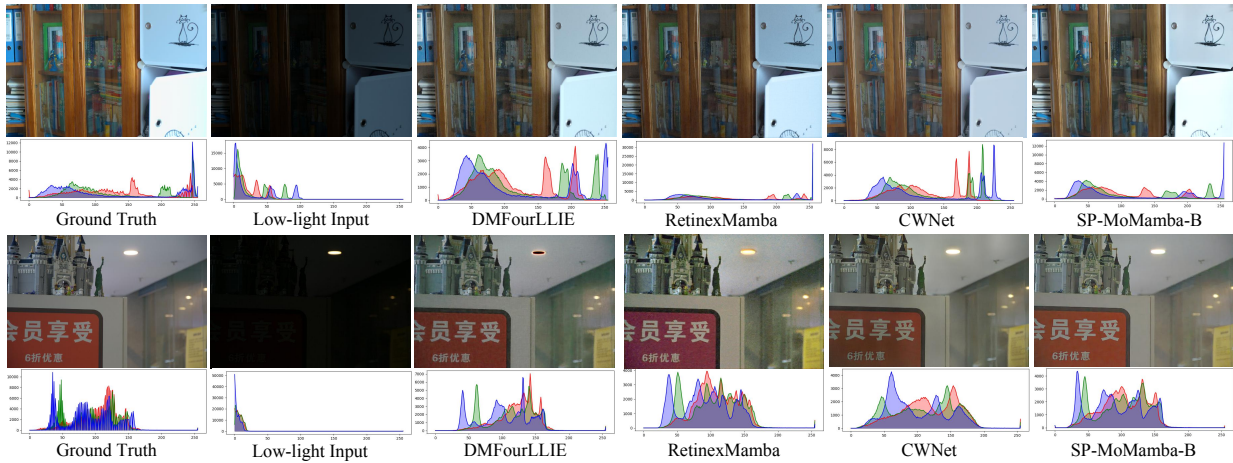


Fig. 15: Qualitative comparisons with existing LLIE methods on the real-world test set LOLv1 and LOLv2-Real [82].

TABLE IX: Analysis of SP-MoMamba generalization. We provide a performance comparison of SP-MoMamba on low-light image enhancement task.

Method	LOLv1		LOLv2-Real	
	PSNR \uparrow	SSIM \uparrow	PSNR \uparrow	SSIM \uparrow
UHDFour [67]	22.89	0.8147	19.42	0.7896
Retinexformer [68]	22.71	0.8177	22.79	0.8397
DMFourLLIE [69]	22.98	0.8273	22.71	0.8583
UHDFormer [70]	22.88	0.8370	19.71	0.832
RetinexMamba [71]	23.15	0.8210	21.73	0.829
MambaLLIE [72]	22.80	0.8315	21.85	0.8276
CWNet [73]	<u>23.60</u>	0.8496	23.31	<u>0.8641</u>
CIDNet [74]	23.81	0.8574	<u>23.43</u>	0.8622
SP-MoMamba-T	23.25	<u>0.8570</u>	23.82	0.8722

work displays a diverse range of expert choices ($\mathcal{E}_1, \mathcal{E}_2, \mathcal{E}_3$) that varies across different network depths and adapts to specific upscaling tasks ($\times 2$ vs. $\times 4$) and datasets. This directly confirms the hierarchical nature of our feature learning process. Specifically, some residual groups select experts with larger scales (e.g., \mathcal{E}_3) to capture global dependencies, while others rely on smaller scales (e.g., \mathcal{E}_1) to recover fine

TABLE X: Quantitative comparison of PSNR on gaussian color image denoising $\sigma = 15$ with state-of-the-art methods.

Method	CBSD68	Kodak24	McMaster	Urban100
FFDNet [75]	33.87	34.63	34.66	33.83
DnCNN [76]	33.90	34.60	33.45	32.98
DRUNet [77]	34.30	35.31	35.40	34.81
SwinIR [4]	34.42	35.34	35.61	35.13
Restormer [78]	34.40	35.35	35.61	35.13
Xformer [79]	34.43	35.39	35.68	35.29
MambaIR [11]	34.48	35.42	35.70	35.37
MambaIRv2 [20]	34.48	35.43	35.73	35.42
SP-MoMamba	34.51	35.44	35.74	35.45

local details. Therefore, using a fixed scale is limiting: it either causes unnecessary computation or struggles to handle complex image structures. Our design allows the network to dynamically adjust the processing scale, finding a balance between restoration performance and computational efficiency.

To better demonstrate this, Fig. 14(b) visualizes the routing choices and intermediate feature maps for an example image from the Urban100 dataset. The router effectively switches between different experts over the network’s depth, taking full advantage of their complementary strengths. As the depth

TABLE XI: Quantitative comparison on JPEG compression artifact reduction under different quality factors q .

Dataset	q	RNAN [80]		RDN [81]		DRUNet [77]		SwinIR [4]		MambaIR [11]		MambaIRv2 [20]		SP-MoMamba	
		PSNR	SSIM	PSNR	SSIM	PSNR	SSIM	PSNR	SSIM	PSNR	SSIM	PSNR	SSIM	PSNR	SSIM
Classic5	10	29.96	0.8178	30.00	0.8188	30.16	0.8234	30.27	0.8249	30.27	0.8256	30.37	0.8269	30.41	0.8271
	30	33.38	0.8924	33.43	0.8930	33.59	0.8949	33.73	0.8961	33.74	0.8965	33.81	0.8970	33.85	0.8972
	40	34.27	0.9061	34.27	0.9061	34.41	0.9075	34.52	0.9082	34.53	0.9084	34.64	0.9093	34.68	0.9096
LIVE1	10	29.63	0.8239	29.67	0.8247	29.79	0.8278	29.86	0.8287	29.88	0.8301	29.91	0.8301	29.94	0.8303
	30	33.45	0.9149	33.51	0.9153	33.59	0.9166	33.69	0.9174	33.72	0.9179	33.73	0.9179	33.77	0.9181
	40	34.47	0.9299	34.51	0.9302	34.58	0.9312	34.67	0.9317	34.70	0.9320	34.73	0.9323	34.78	0.9325

increases, the network becomes highly capable of integrating these multi-scale features to produce high-quality image restorations.

H. Generalization on Other Restoration Tasks

To evaluate the generalization capability of our method, we extend its application to multiple image restoration tasks beyond super-resolution, including low-light image enhancement (LLIE), Gaussian color image denoising, and JPEG compression artifact reduction.

Low-Light Image Enhancement. As shown in Table IX, we compare SP-MoMamba-T against comprehensive state-of-the-art approaches, including Transformer-based (e.g., Retinexformer [68], UHDFormer [70]) and CNN-based (e.g., UHDFour [67], DMFourLLIE [64], CIDNet [74]) and Mamba-based (e.g. RetinexMamba [71], MambaLLIE [72], CWNet [73]) models on the LOLv1 and LOLv2-Real datasets [82]. Our model demonstrates clear improvements, particularly on the more challenging LOLv2-Real benchmark. Specifically, SP-MoMamba-T outperforms the competitive CIDNet method on LOLv2-Real, achieving improvements of 0.39 dB in PSNR and 0.010 in SSIM. We attribute this to the strong global modeling capability of our superpixel-based architecture, which effectively restores illumination while preserving structural details. Furthermore, the visual comparisons in Fig. 15 confirm that our method successfully recovers visibility and accurate color distributions in real-world dark scenarios.

Gaussian Color Image Denoising. To further validate the versatility of SP-MoMamba, we conduct experiments on the Gaussian color image denoising task at noise level $\sigma = 15$, as reported in Table X. We compare our method against a broad set of representative baselines, including CNN-based methods (FFDNet [75], DnCNN [76], DRUNet [77]), Transformer-based methods (SwinIR [4], Restormer [78], Xformer [79]), and Mamba-based methods (MambaIR [11], MambaIRv2 [20]), evaluated on four standard benchmarks: CBSD68, Kodak24, McMaster, and Urban100. SP-MoMamba consistently achieves the highest PSNR scores across all four datasets. Notably, SP-MoMamba surpasses MambaIRv2 by 0.03 dB on CBSD68, 0.01 dB on Kodak24, 0.01 dB on McMaster, and 0.03 dB on Urban100, demonstrating that the proposed superpixel-driven semantic scanning mechanism benefits not only super-resolution tasks but also noise suppression tasks that require precise preservation of structural boundaries and texture fidelity. The consistent improvement across all benchmarks reflects that grouping semantically coherent pixels into superpixel tokens effectively guides the model to distinguish between genuine image structures and noise patterns during restoration.

JPEG Compression Artifact Reduction. We further evaluate SP-MoMamba on the task of JPEG compression artifact reduction under multiple quality factors ($q = 10, 30, 40$) on the Classic5 and LIVE1 benchmark datasets, as presented in Table XI. We compare against RNAN [80], RDN [81], DRUNet [77], SwinIR [4], MambaIR [11], and MambaIRv2 [20]. SP-MoMamba achieves state-of-the-art performance across all quality factors and both datasets. On Classic5, our method reaches 30.41/0.8271, 33.85/0.8972, and 34.68/0.9096 in PSNR/SSIM under $q = 10, 30$, and 40, respectively, consistently outperforming MambaIRv2, which was the previous best-performing method. Similarly, on LIVE1, SP-MoMamba attains 29.94/0.8303, 33.77/0.9181, and 34.78/0.9325 under the three quality settings, again surpassing all compared baselines. The performance gains are particularly notable at the most challenging low-quality setting ($q = 10$), where JPEG blocking artifacts are most severe. This suggests that the multi-scale superpixel representation in SP-MoMamba is well-suited for identifying and eliminating structured compression artifacts, as the superpixel clustering naturally aligns with semantic object boundaries and can better distinguish genuine image content from compression-induced distortions.

Overall, these results across three diverse restoration tasks—low-light enhancement, Gaussian denoising, and JPEG artifact reduction—highlight the flexibility and strong generalization potential of our design beyond standard super-resolution, confirming that the superpixel-driven state space modeling paradigm is broadly effective for image restoration.

VI. CONCLUSION

In this study, we propose SP-MoMamba, a superpixel-driven mixture of state space experts model. Unlike the other state space models, SP-MoMamba addresses the computational inefficiencies inherent in existing mamba-based restoration methods dependent on global scanning by integrating superpixel sampling with state space frameworks. This approach effectively balances robust global semantic modeling with precise local detail enhancement while minimizing complexity. In our method, the MSS-MoE module achieves comprehensive global modeling by dynamically selecting optimal experts across multiple scales, while the LSME refines local features through a synergistic combination of self-attention and channel attention mechanisms. Experimental results confirm that SP-MoMamba surpasses state-of-the-art lightweight models across various benchmark datasets.

REFERENCES

- [1] C. Dong, C. C. Loy, K. He, and X. Tang, "Image super-resolution using deep convolutional networks," *IEEE transactions on pattern analysis and machine intelligence*, vol. 38, no. 2, pp. 295–307, 2015.

- [2] B. Lim, S. Son, H. Kim, S. Nah, and K. M. Lee, "Enhanced deep residual networks for single image super-resolution," in *2017 IEEE Conference on Computer Vision and Pattern Recognition Workshops (CVPRW)*, 2017, pp. 1132–1140.
- [3] Y. Zhang, K. Li, K. Li, L. Wang, B. Zhong, and Y. Fu, "Image super-resolution using very deep residual channel attention networks," in *Proceedings of the European conference on computer vision (ECCV)*, 2018, pp. 286–301.
- [4] J. Liang, J. Cao, G. Sun, K. Zhang, L. Van Gool, and R. Timofte, "Swinir: Image restoration using swin transformer," in *Proceedings of the IEEE/CVF international conference on computer vision*, 2021, pp. 1833–1844.
- [5] Y. Li, Y. Fan, X. Xiang, D. Demandolx, R. Ranjan, R. Timofte, and L. Van Gool, "Efficient and explicit modelling of image hierarchies for image restoration," in *Proceedings of the IEEE/CVF Conference on Computer Vision and Pattern Recognition (CVPR)*, June 2023, pp. 18 278–18 289.
- [6] Y. Zhou, Z. Li, C.-L. Guo, S. Bai, M.-M. Cheng, and Q. Hou, "Srfornet: Permuted self-attention for single image super-resolution," in *Proceedings of the IEEE/CVF International Conference on Computer Vision*, 2023, pp. 12 780–12 791.
- [7] X. Chu, B. Zhang, H. Ma, R. Xu, and Q. Li, "Fast, accurate and lightweight super-resolution with neural architecture search," in *2020 25th International conference on pattern recognition (ICPR)*. IEEE, 2021, pp. 59–64.
- [8] Y. Tai, J. Yang, and X. Liu, "Image super-resolution via deep recursive residual network," in *Proceedings of the IEEE conference on computer vision and pattern recognition*, 2017, pp. 3147–3155.
- [9] J. Liu, J. Tang, and G. Wu, "Residual feature distillation network for lightweight image super-resolution," in *Computer vision—ECCV 2020 workshops: Glasgow, UK, August 23–28, 2020, proceedings, part III 16*. Springer, 2020, pp. 41–55.
- [10] Z. Hui, X. Wang, and X. Gao, "Fast and accurate single image super-resolution via information distillation network," in *Proceedings of the IEEE conference on computer vision and pattern recognition*, 2018, pp. 723–731.
- [11] H. Guo, J. Li, T. Dai, Z. Ouyang, X. Ren, and S.-T. Xia, "Mambair: A simple baseline for image restoration with state-space model," in *European conference on computer vision*. Springer, 2024, pp. 222–241.
- [12] A. Gu and T. Dao, "Mamba: Linear-time sequence modeling with selective state spaces," *arXiv preprint arXiv:2312.00752*, 2023.
- [13] Y. Liu, Y. Tian, Y. Zhao, H. Yu, L. Xie, Y. Wang, Q. Ye, and Y. Liu, "Vmamba: Visual state space model," *arXiv preprint arXiv:2401.10166*, 2024.
- [14] L. Zhu, B. Liao, Q. Zhang, X. Wang, W. Liu, and X. Wang, "Vision mamba: Efficient visual representation learning with bidirectional state space model," *arXiv preprint arXiv:2401.09417*, 2024.
- [15] G. Zhang, L. Fan, C. He, Z. Lei, Z.-X. ZHANG, and L. Zhang, "Voxel mamba: Group-free state space models for point cloud based 3d object detection," *Advances in Neural Information Processing Systems*, vol. 37, pp. 81 489–81 509, 2025.
- [16] Z. Wang, C. Li, H. Xu, and X. Zhu, "Mamba yolo: Ssms-based yolo for object detection," *arXiv preprint arXiv:2406.05835*, 2024.
- [17] J. Qiao, J. Liao, W. Li, Y. Zhang, Y. Guo, Y. Wen, Z. Qiu, J. Xie, J. Hu, and S. Lin, "Hi-mamba: Hierarchical mamba for efficient image super-resolution," *arXiv preprint arXiv:2410.10140*, 2024.
- [18] W. Zou, H. Gao, W. Yang, and T. Liu, "Wave-mamba: Wavelet state space model for ultra-high-definition low-light image enhancement," in *Proceedings of the 32nd ACM International Conference on Multimedia*, 2024, pp. 1534–1543.
- [19] Z. Zhen, Y. Hu, and Z. Feng, "Freqmamba: Viewing mamba from a frequency perspective for image deraining," *arXiv preprint arXiv:2404.09476*, 2024.
- [20] H. Guo, Y. Guo, Y. Zha, Y. Zhang, W. Li, T. Dai, S.-T. Xia, and Y. Li, "Mambairv2: Attentive state space restoration," in *Proceedings of the Computer Vision and Pattern Recognition Conference*, 2025, pp. 28 124–28 133.
- [21] L. Kong, J. Dong, J. Tang, M.-H. Yang, and J. Pan, "Efficient visual state space model for image deblurring," in *Proceedings of the IEEE/CVF Conference on Computer Vision and Pattern Recognition (CVPR)*, June 2025, pp. 12 710–12 719.
- [22] J. Wagemans, J. H. Elder, M. Kubovy, S. E. Palmer, M. A. Peterson, M. Singh, and R. Von der Heydt, "A century of gestalt psychology in visual perception: I. perceptual grouping and figure–ground organization," *Psychological bulletin*, vol. 138, no. 6, p. 1172, 2012.
- [23] W. Shi, J. Caballero, F. Huszár, J. Totz, A. P. Aitken, R. Bishop, D. Rueckert, and Z. Wang, "Real-time single image and video super-resolution using an efficient sub-pixel convolutional neural network," in *2016 IEEE Conference on Computer Vision and Pattern Recognition (CVPR)*, 2016, pp. 1874–1883.
- [24] W. Zou, L. Chen, Y. Wu, Y. Zhang, Y. Xu, and J. Shao, "Joint wavelet sub-bands guided network for single image super-resolution," *IEEE Transactions on Multimedia*, vol. 25, pp. 4623–4637, 2022.
- [25] J. Kim, J. K. Lee, and K. M. Lee, "Accurate image super-resolution using very deep convolutional networks," in *2016 IEEE Conference on Computer Vision and Pattern Recognition (CVPR)*, 2016, pp. 1646–1654.
- [26] Z. Liu, Y. Lin, Y. Cao, H. Hu, Y. Wei, Z. Zhang, S. Lin, and B. Guo, "Swin transformer: Hierarchical vision transformer using shifted windows," in *Proceedings of the IEEE/CVF international conference on computer vision*, 2021, pp. 10 012–10 022.
- [27] J. Zhang, Y. Zhang, J. Gu, Y. Zhang, L. Kong, and X. Yuan, "Accurate image restoration with attention retractable transformer," *arXiv preprint arXiv:2210.01427*, 2022.
- [28] H. Wang, X. Chen, B. Ni, Y. Liu, and J. Liu, "Omni aggregation networks for lightweight image super-resolution," in *Proceedings of the IEEE/CVF Conference on Computer Vision and Pattern Recognition*, 2023, pp. 22 378–22 387.
- [29] N. Ahn, B. Kang, and K.-A. Sohn, "Fast, accurate, and lightweight super-resolution with cascading residual network," in *Proceedings of the European conference on computer vision (ECCV)*, 2018, pp. 252–268.
- [30] L. Sun, J. Dong, J. Tang, and J. Pan, "Spatially-adaptive feature modulation for efficient image super-resolution," in *Proceedings of the IEEE/CVF international conference on computer vision*, 2023, pp. 13 190–13 199.
- [31] X. Zhang, H. Zeng, S. Guo, and L. Zhang, "Efficient long-range attention network for image super-resolution," in *European conference on computer vision*. Springer, 2022, pp. 649–667.
- [32] Z. Lu, J. Li, H. Liu, C. Huang, L. Zhang, and T. Zeng, "Transformer for single image super-resolution," in *Proceedings of the IEEE/CVF conference on computer vision and pattern recognition*, 2022, pp. 457–466.
- [33] W. Zou, T. Ye, W. Zheng, Y. Zhang, L. Chen, and Y. Wu, "Self-calibrated efficient transformer for lightweight super-resolution," in *Proceedings of the IEEE/CVF conference on computer vision and pattern recognition*, 2022, pp. 930–939.
- [34] A. Zhang, W. Ren, Y. Liu, and X. Cao, "Lightweight image super-resolution with superpixel token interaction," in *Proceedings of the IEEE/CVF international conference on computer vision*, 2023, pp. 12 728–12 737.
- [35] C. Wu, L. Wang, Z. Zheng, Y. Cui, Z. Yang, X. Chen, Y. Zhang, W. Jiang, and J. Xia, "Scan clusters, not pixels: A cluster-centric paradigm for efficient ultra-high-definition image restoration," *arXiv preprint arXiv:2602.21917*, 2026.
- [36] C. Riquelme, J. Puigcerver, B. Mustafa, M. Neumann, R. Jenatton, A. Susano Pinto, D. Keysers, and N. Houlsby, "Scaling vision with sparse mixture of experts," *Advances in Neural Information Processing Systems*, vol. 34, pp. 8583–8595, 2021.
- [37] L. Wu, M. Liu, Y. Chen, D. Chen, X. Dai, and L. Yuan, "Residual mixture of experts," *arXiv preprint arXiv:2204.09636*, 2022.
- [38] M. Emad, M. Peemen, and H. Corporaal, "Moesr: Blind super-resolution using kernel-aware mixture of experts," in *Proceedings of the IEEE/CVF Winter Conference on Applications of Computer Vision*, 2022, pp. 3408–3417.
- [39] E. Zamfir, Z. Wu, N. Mehta, Y. Zhang, and R. Timofte, "See more details: Efficient image super-resolution by experts mining," in *Forty-first International Conference on Machine Learning*, 2024.
- [40] L. Rossi, V. Bernuzzi, T. Fontanini, M. Bertozzi, and A. Prati, "Swin2-mose: A new single image supersolution model for remote sensing," *IET Image Processing*, vol. 19, no. 1, p. e13303, 2025.
- [41] J. Liang, H. Zeng, and L. Zhang, "Efficient and degradation-adaptive network for real-world image super-resolution," in *European Conference on Computer Vision*. Springer, 2022, pp. 574–591.
- [42] M. V. Conde, U.-J. Choi, M. Burchi, and R. Timofte, "Swin2sr: Swin2 transformer for compressed image super-resolution and restoration," in *European Conference on Computer Vision*. Springer, 2022, pp. 669–687.
- [43] J. Gu and C. Dong, "Interpreting super-resolution networks with local attribution maps," in *Proceedings of the IEEE/CVF conference on computer vision and pattern recognition*, 2021, pp. 9199–9208.
- [44] Z. Chen, Y. Zhang, J. Gu, L. Kong, X. Yang, and F. Yu, "Dual aggregation transformer for image super-resolution," in *Proceedings of*

- the *IEEE/CVF international conference on computer vision*, 2023, pp. 12 312–12 321.
- [45] N. Shazeer, “Glu variants improve transformer,” *arXiv preprint arXiv:2002.05202*, 2020.
- [46] E. Jang, S. Gu, and B. Poole, “Categorical reparameterization with gumbel-softmax,” *arXiv preprint arXiv:1611.01144*, 2016.
- [47] V. Jampani, D. Sun, M.-Y. Liu, M.-H. Yang, and J. Kautz, “Supersampling networks,” in *Proceedings of the European Conference on Computer Vision (ECCV)*, 2018, pp. 352–368.
- [48] H. Zhao, X. Kong, J. He, Y. Qiao, and C. Dong, “Efficient image super-resolution using pixel attention,” in *Computer Vision—ECCV 2020 Workshops: Glasgow, UK, August 23–28, 2020, Proceedings, Part III 16*. Springer, 2020, pp. 56–72.
- [49] K. Park, J. W. Soh, and N. I. Cho, “A dynamic residual self-attention network for lightweight single image super-resolution,” *IEEE Transactions on Multimedia*, vol. 25, pp. 907–918, 2021.
- [50] F. Huang, H. Liu, L. Chen, Y. Shen, and M. Yu, “Feature enhanced cascading attention network for lightweight image super-resolution,” *Scientific Reports*, vol. 15, no. 1, p. 20511, 2025.
- [51] F. Li, R. Cong, J. Wu, H. Bai, M. Wang, and Y. Zhao, “Sronvnet: A transformer-style convnet for lightweight image super-resolution,” *International Journal of Computer Vision*, vol. 133, no. 1, pp. 173–189, 2025.
- [52] G. Wu, J. Jiang, J. Jiang, and X. Liu, “Transforming image super-resolution: A convformer-based efficient approach,” *IEEE Transactions on Image Processing*, 2024.
- [53] R. Timofte, E. Agustsson, L. V. Gool, M. Yang, L. Zhang, B. Lim, S. Son, H. Kim, S. Nah, and K. M. L. et al., “Ntire 2017 challenge on single image super-resolution: Methods and results,” in *2017 IEEE Conference on Computer Vision and Pattern Recognition Workshops (CVPRW)*, 2017, pp. 1110–1121.
- [54] M. Bevilacqua, A. Roumy, C. Guillemot, and M. L. Alberi-Morel, “Low-complexity single-image super-resolution based on nonnegative neighbor embedding,” 2012.
- [55] R. Zeyde, M. Elad, and M. Protter, “On single image scale-up using sparse-representations,” 2010.
- [56] D. Martin, C. Fowlkes, D. Tal, and J. Malik, “A database of human segmented natural images and its application to evaluating segmentation algorithms and measuring ecological statistics,” in *Proceedings Eighth IEEE International Conference on Computer Vision. ICCV 2001*, vol. 2, 2001, pp. 416–423 vol.2.
- [57] J. Huang, A. Singh, and N. Ahuja, “Single image super-resolution from transformed self-exemplars,” in *2015 IEEE Conference on Computer Vision and Pattern Recognition (CVPR)*, 2015, pp. 5197–5206.
- [58] Y. Matsui, K. Ito, Y. Aramaki, T. Yamasaki, and K. Aizawa, “Sketch-based manga retrieval using manga109 dataset,” 2015.
- [59] L. Sun, J. Pan, and J. Tang, “Shufflemixer: An efficient convnet for image super-resolution,” *Advances in Neural Information Processing Systems*, vol. 35, pp. 17 314–17 326, 2022.
- [60] D. P. Kingma and J. Ba, “Adam: A method for stochastic optimization,” *arXiv preprint arXiv:1412.6980*, 2014.
- [61] J. Cai, H. Zeng, H. Yong, Z. Cao, and L. Zhang, “Toward real-world single image super-resolution: A new benchmark and a new model,” in *Proceedings of the IEEE/CVF international conference on computer vision*, 2019, pp. 3086–3095.
- [62] Y. Wang, Y. Liu, S. Zhao, J. Li, and L. Zhang, “Camixers: Only details need more” attention,” in *Proceedings of the IEEE/CVF Conference on Computer Vision and Pattern Recognition*, 2024, pp. 25 837–25 846.
- [63] A. Li, L. Zhang, Y. Liu, and C. Zhu, “Exploring frequency-inspired optimization in transformer for efficient single image super-resolution,” *IEEE Transactions on Pattern Analysis and Machine Intelligence*, 2025.
- [64] W. Li, H. Guo, Y. Hou, G. Gao, and Z. Ma, “Dual-domain modulation network for lightweight image super-resolution,” *IEEE Transactions on Multimedia*, pp. 1–11, 2026.
- [65] R. Achanta, A. Shaji, K. Smith, A. Lucchi, P. Fua, and S. Süsstrunk, “Slic superpixels compared to state-of-the-art superpixel methods,” *IEEE transactions on pattern analysis and machine intelligence*, vol. 34, no. 11, pp. 2274–2282, 2012.
- [66] H. Huang, X. Zhou, J. Cao, R. He, and T. Tan, “Vision transformer with super token sampling,” *arXiv preprint arXiv:2211.11167*, 2022.
- [67] C. Li, C.-L. Guo, M. Zhou, Z. Liang, S. Zhou, R. Feng, and C. C. Loy, “Embedding fourier for ultra-high-definition low-light image enhancement,” *arXiv preprint arXiv:2302.11831*, 2023.
- [68] Y. Cai, H. Bian, J. Lin, H. Wang, R. Timofte, and Y. Zhang, “Retinexformer: One-stage retinex-based transformer for low-light image enhancement,” in *Proceedings of the IEEE/CVF international conference on computer vision*, 2023, pp. 12 504–12 513.
- [69] T. Zhang, P. Liu, M. Zhao, and H. Lv, “Dmfourllie: dual-stage and multi-branch fourier network for low-light image enhancement,” in *Proceedings of the 32nd ACM International Conference on Multimedia*, 2024, pp. 7434–7443.
- [70] C. Wang, J. Pan, W. Wang, G. Fu, S. Liang, M. Wang, X.-M. Wu, and J. Liu, “Correlation matching transformation transformers for uhd image restoration,” in *Proceedings of the AAAI Conference on Artificial Intelligence*, vol. 38, no. 6, 2024, pp. 5336–5344.
- [71] J. Bai, Y. Yin, Q. He, Y. Li, and X. Zhang, “Retinexmamba: Retinex-based mamba for low-light image enhancement,” in *International Conference on Neural Information Processing*. Springer, 2024, pp. 427–442.
- [72] J. Weng, Z. Yan, Y. Tai, J. Qian, J. Yang, and J. Li, “Mamballie: Implicit retinex-aware low light enhancement with global-then-local state space,” *Advances in Neural Information Processing Systems*, vol. 37, pp. 27 440–27 462, 2024.
- [73] T. Zhang, P. Liu, Y. Lu, M. Cai, Z. Zhang, Z. Zhang, and Q. Zhou, “Cwnet: Causal wavelet network for low-light image enhancement,” in *Proceedings of the IEEE/CVF International Conference on Computer Vision*, 2025, pp. 8789–8799.
- [74] Q. Yan, K. Shi, Y. Feng, T. Hu, P. Wu, G. Pang, and Y. Zhang, “Hvidnet+: Beyond extreme darkness for low-light image enhancement,” *arXiv preprint arXiv:2507.06814*, 2025.
- [75] K. Zhang, W. Zuo, S. Gu, and L. Zhang, “Learning deep cnn denoiser prior for image restoration,” in *Proceedings of the IEEE conference on computer vision and pattern recognition*, 2017, pp. 3929–3938.
- [76] K. Zhang, W. Zuo, Y. Chen, D. Meng, and L. Zhang, “Beyond a gaussian denoiser: Residual learning of deep cnn for image denoising,” *IEEE transactions on image processing*, vol. 26, no. 7, pp. 3142–3155, 2017.
- [77] K. Zhang, Y. Li, W. Zuo, L. Zhang, L. Van Gool, and R. Timofte, “Plug-and-play image restoration with deep denoiser prior,” *IEEE Transactions on Pattern Analysis and Machine Intelligence*, vol. 44, no. 10, pp. 6360–6376, 2021.
- [78] S. W. Zamir, A. Arora, S. Khan, M. Hayat, F. S. Khan, and M.-H. Yang, “Restormer: Efficient transformer for high-resolution image restoration,” in *Proceedings of the IEEE/CVF conference on computer vision and pattern recognition*, 2022, pp. 5728–5739.
- [79] J. Zhang, Y. Zhang, J. Gu, J. Dong, L. Kong, and X. Yang, “Xformer: Hybrid x-shaped transformer for image denoising,” in *International Conference on Learning Representations*, vol. 2024, 2024, pp. 13 333–13 345.
- [80] Y. Zhang, K. Li, K. Li, B. Zhong, and Y. Fu, “Residual non-local attention networks for image restoration,” *arXiv preprint arXiv:1903.10082*, 2019.
- [81] Y. Zhang, Y. Tian, Y. Kong, B. Zhong, and Y. Fu, “Residual dense network for image super-resolution,” in *Proceedings of the IEEE conference on computer vision and pattern recognition*, 2018, pp. 2472–2481.
- [82] C. Wei, W. Wang, W. Yang, and J. Liu, “Deep retinex decomposition for low-light enhancement,” *arXiv preprint arXiv:1808.04560*, 2018.

Wenbin Zou received the master's degree with the College of Photonic and Electronic Engineering, Fujian Normal University, Fuzhou, China, in 2022. He is currently pursuing joint Ph.D. dual degree with the Shien-Ming Wu School of Intelligent Engineering, South China University of Technology, Guangzhou, China, and with the Department of Electrical and Electronic Engineering, The Hong Kong Polytechnic University, Hong Kong SAR. His research interests include Low-light Image Enhancement, signal image super resolution and related vision problems.

Yawen Cui received B.E. degree in computer science and technology from Jiangnan University, Wuxi, China, and the M.S. degree in software engineering from the National University of Defense Technology (NUDT), Changsha, China, in 2016 and 2019, respectively, and the Ph.D. degree from the University of Oulu, Finland, in 2023. She is currently a postdoctoral researcher at the Department of Electrical and Electronic Engineering, The Hong Kong Polytechnic University, Hong Kong. Her research interests include few-shot learning, continual learning and multimodal learning.

Yi Wang (Member, IEEE) received BEng degree in electronic information engineering and MEng degree in information and signal processing from the School of Electronics and Information, Northwestern Polytechnical University, Xi'an, China, in 2013 and 2016, respectively. He earned a PhD in the School of Electrical and Electronic Engineering from Nanyang Technological University, Singapore, in 2021. He is currently a Research Assistant Professor in the Department of Electrical and Electronic Engineering at The Hong Kong Polytechnic University, Hong Kong. His research interests include Image/Video Processing, Egocentric Vision, Embodied Intelligence, and Trustworthy AI.

Lap-Pui Chau (Fellow, IEEE) received a Ph.D. degree from The Hong Kong Polytechnic University in 1997. He was with the School of Electrical and Electronic Engineering, Nanyang Technological University from 1997 to 2022. He is currently a Professor in the Department of Electrical and Electronic Engineering, The Hong Kong Polytechnic University. His current research interests include image and video analytics and autonomous driving. He is an IEEE Fellow. He was the chair of Technical Committee on Circuits & Systems for Communications of IEEE Circuits and Systems Society from 2010 to 2012. He was general chairs and program chairs for some international conferences. Besides, he served as associate editors for several IEEE journals and Distinguished Lecturer for IEEE BTS.

Liang Chen received the Ph.D. degree in communication and information systems from NERCMS, Wuhan University, China, in 2017, and the joint Ph.D. degree in computer science from the City University of Hong Kong, Hong Kong, in 2018. She is currently an Associate Professor with Fujian Normal University, Fuzhou, China. Her research interests include image super resolution and related vision problems.

Jinshan Pan (Senior Member, IEEE) received the PhD degree in computational mathematics from the Dalian University of Technology, China, in 2017. He was a joint-training PhD student with the School of Mathematical Sciences, Dalian University of Technology and also with Electrical Engineering and Computer Science, University of California, Merced, CA. He is currently a professor with the School of Computer Science and Engineering, Nanjing University of Science and Technology. His research interests include image deblurring, image/video analysis and enhancement, and related vision problems. He is a senior member of IEEE.

Huiping Zhuang (Member, IEEE) received his PhD from Nanyang Technological University, Singapore in 2021 and was recognized with the National Outstanding Overseas Student Award of China. He leads key projects including the National Key R&D Program of China and National Natural Science Foundation projects. His research focuses on efficient AI (including efficient continual learning and embodied intelligence), with around 80 published papers. He pioneered "Analytic Continual Learning," establishing a new branch in evolvable intelligence. His works have been recognized with 2 Best Paper Awards (nomination) at international conferences, the Best Student Paper Achievement Award from Singapore's PREMIA Association, and a First Prize at the CVPR 2025 competition. He has delivered a keynote speech at an international conference and served in academic roles (e.g., Co-Chair) at several international/domestic conferences. He serves as a special issue editor for the Journal of Franklin Institute (JCR Q1) and was recognized as an Outstanding Reviewer for ICML 2022.

Guanbin Li (Member, IEEE) is currently a full professor in School of Computer Science and Engineering, Sun Yat-sen University. He received his PhD degree from the University of Hong Kong in 2016. His current research interests include computer vision, image processing, and deep learning. He is a recipient of the ICCV 2019 Best Paper Nomination Award and CVPR 2024 best paper candidate. He has authorized and co-authored on more than 200 papers in top-tier academic journals and conferences. He serves as an area chair for the conference of CVPR and ICCV.